MATERIALS SCIENCE

In vivo hitchhiking of immune cells by intracellular self-assembly of bacteria-mimetic nanomedicine for targeted therapy of melanoma

Cheng Gao[1,2]†, Qingfu Wang[1]†, Junyan Li[1], Cheryl H. T. Kwong[1], Jianwen Wei[1], Beibei Xie[1], Siyu Lu[3], Simon M. Y. Lee[1,2]*, Ruibing Wang[1,2]*

Cell-based drug carriers are mostly prepared in vitro, which may negatively affect the physiological functions of cells, and induce possible immune rejections when applied to different individuals. In addition, the immunosuppressive tumor microenvironment limits immune cell–mediated delivery. Here, we report an in vivo strategy to construct cell-based nanomedicine carriers, where bacteria-mimetic gold nanoparticles (GNPs) are intravenously injected, selectively phagocytosed by phagocytic immune cells, and subsequently self-assemble into sizable intracellular aggregates via host-guest interactions. The intracellular aggregates minimize exocytosis of GNPs from immune cells and activate the photothermal property via plasmonic coupling effects. Phagocytic immune cells carry the intracellular GNP aggregates to melanoma tissue via inflammatory tropism. Moreover, an initial photothermal treatment (PTT) of the tumor induces tumor damage that subsequently provides positive feedback to recruit more immune cell–based carriers for enhanced targeting efficiency. The optimized secondary PTT notably improves antitumor immunotherapy, further strengthened by immune checkpoint blockade.

INTRODUCTION

In recent years, cell-based drug delivery systems have emerged, which combines the unique physiological properties (e.g., the high biocompatibility and homing effects) of endogenous cells and the physicochemical properties of synthetic formulations (*1*–*3*). Cell-based carriers can disguise payload as a "self" component during systemic circulation and help it escape the clearance of the reticuloendothelial system, thereby improving the utilization of drugs (*4*–*6*). For instance, Mitragotri and coworkers (*7*) designed an erythrocyte-based immune targeting system, which delivers antigenic nanoparticles anchored on the surface of the carrier cells to the antigen-presenting cells in the spleen. For some diseased tissues that are difficult for medicines to reach (such as myeloma and brain cancer), the homing effects of stem cells and the inflammatory tropism of immune cells were usually used to develop cell-based carrier to improve targeted delivery (*8*–*11*). Gu and coworkers covalently attached platelets (anti–PD-1 antibody on the surface) to the surface of hematopoietic stem cells (HSCs) via click chemistry, and HSC brought the platelets into the bone marrow due to the homing effects of HSC (*12*). Subsequently, the tumor microenvironment stimulated the platelets to release anti–PD-1 antibody for immunotherapy of leukemia (*12*). Very recently, Wang *et al.* (*13*) developed a cell-friendly, facile host-guest interaction-mediated macrophage-liposome conjugation strategy for macrophage-hitchhiking delivery of medicine to treat inflammatory diseases. In all of these previously reported examples, the cell-based carriers were constructed in vitro before in vivo administration, which often requires separation of endogenous cells, and large-scale preparation is barely possible (*14*, *15*). The subsequent drug loading processes, via either intracellular drug internalization or cell surface attachment, may inevitably affect the physiological function of the carrier cells (*16*). Last, the isolated and subsequently prepared transporting cells only correspond to one single host, and it would still generate immune rejection when applied to other individuals (*17*, *18*). Moreover, drug leakage from cell-based carriers often takes place during in vivo delivery, which may negatively affect the overall targeting efficiency (*19*).

The other key factor of cell-based carrier was the targeted delivery efficiency mediated by cell's physiological function. Recently, Wang *et al.* (*15*) have demonstrated that nanomedicine-loaded macrophage could be accumulated in the aorta atherosclerotic plaque through inflammation tropism–mediated active targeting and significantly promoted atherosclerotic regression. The inflammation tropism–mediated active targeting of immune cells was attributed to the chemoattractant difference between the systemic circulation and disease site (*20*). Thus, inflammation plays an essential role for immune cell–based targeted delivery, and most of previous researches also took advantage of this special feature of immune cell to construct cell-based carriers for targeted delivery of therapeutic payloads (*21*, *22*). Although immune cells show better tumor targeting efficiency than traditional nanomedicine, the immunesuppressive microenvironment of tumor often leads to insufficient recruitment of immune cells carriers in the tumor (*23*). Thus far, very few strategies have been developed to improve the targeted delivery efficiency of immune cell–based carriers into solid tumors.

Here we report an in vivo strategy to efficiently and stably hitchhike phagocytic immune cells via selective phagocytosis of bacteria-mimetic gold nanoparticles (GNPs) and their subsequent supramolecular self-assembly intracellularly (Fig. 1). In this design, both β-cyclodextrin (β-CD)–modified GNPs and adamantane (ADA)–modified GNPs are respectively coated by *Escherichia coli* outer membrane vesicles (OMVs). The *E. coli* OMVs induce the phagocytosis of GNPs by circulating immune cells, leading to intracellular degradation of OMVs and subsequent supramolecular self-assembly of GNPs driven by β-CD–ADA host-guest interactions

[1]State Key Laboratory of Quality Research in Chinese Medicine, Institute of Chinese Medical Sciences, University of Macau, Taipa, Macau 999078, China. [2]MoE Frontiers Science Center for Precision Oncology, University of Macau, Taipa, Macau 999078, China. [3]Green Catalysis Center, College of Chemistry and Molecular Engineering, Zhengzhou University, Zhengzhou, 450000, China.
*Corresponding author. Email: rwang@um.edu.mo (R.W.); simonlee@um.edu.mo (S.L.)
†These authors contributed equally to this work.

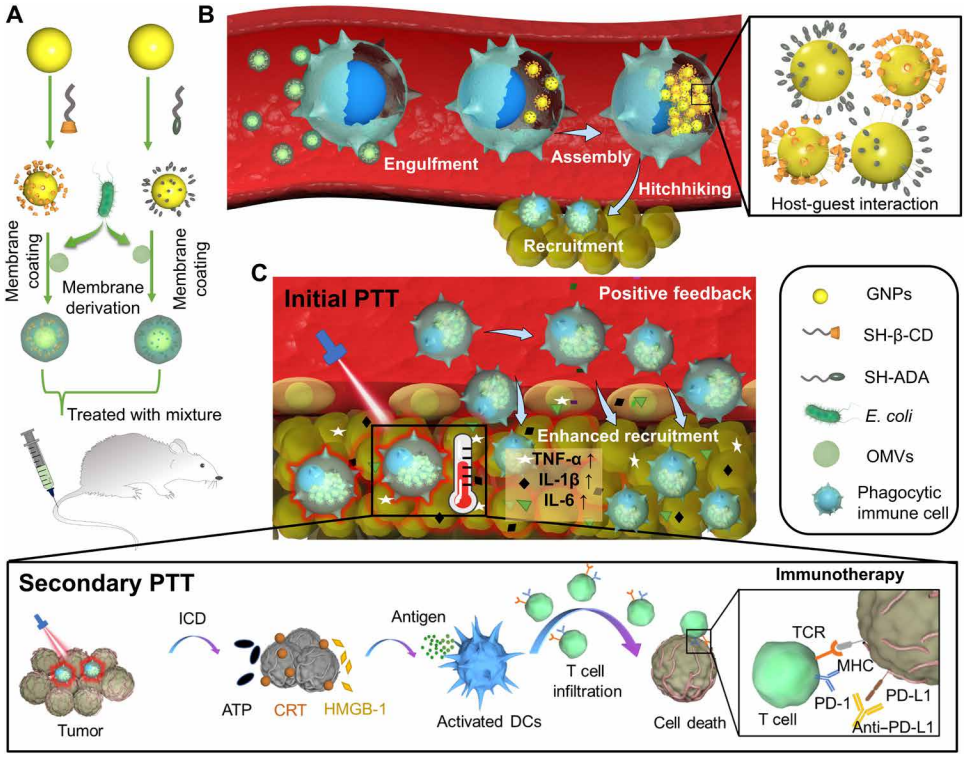

Fig. 1. In vivo construction of immune cell–based nanomedicine carriers and initial PTT treatment enhance hitchhiking delivery into the tumor and improve antitumor immunotherapy. (**A**) *E. coli* OMVs are coated on both CD-GNPs and ADA-GNPs to prepare bacteria-mimetic nanoparticles. (**B**) Selective phagocytosis of bacteria-mimetic nanoparticles by phagocytic immune cells induces OMV degradation and subsequent intracellular aggregation of GNPs mediated by CD-ADA host-guest interactions, leading to photothermal property due to the plasmonic effects of GNP aggregates. The large size of intracellular GNP aggregates also inhibits the leakage during in vivo cell-hitchhiking delivery. Because of the inflammatory tropism to melanoma, immune cells achieve the targeted delivery of intracellular GNP aggregates to the tumor tissues. (**C**) Initial PTT treatment of GNP aggregates induces tumor damage that subsequently enhances inflammatory signals and provides a positive feedback to recruit more immune cells (including the carriers) for enhanced antitumor therapy. Secondary photothermal treatment (PTT) of Mixture induces tumor cell immunogenic cell death (ICD) and activates antitumor immune response, further strengthened by immune checkpoint blockage (aPD-L1).

(*24*). This process turns dispersed GNPs without photothermal effect into GNP aggregates with photothermal effect and significantly inhibits the leakage of GNPs from immune cells. Because of the inflammatory tropism (*25*), immune cells carry the intracellular GNP aggregates to the tumor tissues in vivo. Moreover, to improve the inflammation-mediated targeting efficiency of immune cell–based carriers to the tumor, upon the initial accumulation of GNPs carried by the phagocytic immune cells into the tumor, an initial photothermal treatment (PTT) of the tumor is conducted to induce tumor damage and enhance the tumor inflammatory signals, thereby providing a positive feedback to recruit more immune cells (including carriers that contain intracellular GNP aggregates), leading to significantly improved tumor accumulation of GNP aggregates for secondary PTT treatment. This approach showed highly effective antitumor PTT/immunotherapy, which is further strengthened by an immune checkpoint inhibitor.

RESULTS AND DISCUSSION

PTT of GNP aggregates induced immunogenic tumor cell death

GNPs were synthesized in an aqueous solution by using citrate reduction of chloroauric acid according to reported methods (*26*, *27*) and then reacted with mono (6-mercapto-6-deoxy) β-CD and 1-mercaptoamantane (ADA) via gold-sulfur bond, respectively, affording β-CD–modified GNPs (CD-GNPs) and ADA-modified GNPs (ADA-GNPs; fig. S1). The molar ratios of [CD]/[$AuCl_4^-$] and [ADA]/[$AuCl_4^-$] in the reaction mixtures were both 0.1. As shown in Fig. 2 (A and B), both transmission electronic microscopy (TEM) and scanning electronic microscopy (SEM) analysis exhibited spherical morphology of GNPs with a diameter of ~10 nm. Because of host-guest interactions between β-CD and ADA (Fig. 2C) (*24*, *28*), the mixed solution of CD-GNPs and ADA-GNPs (equivalent Au content) turned black from purple (Fig. 2D), and both TEM and SEM images showed micrometer-sized GNP aggregates (Fig. 2, E and F) with a mean diameter of 2.5 μm (Fig. 2G) and a negative zeta potential (fig. S2A), confirmed by dynamic light scattering (DLS) analysis. Furthermore, a red shift from 540 to 620 nm was detected on the absorption wavelength of GNP aggregates (Fig. 2H), and the temperature increased up to 48°C after near infrared (NIR) irradiation with an 808-nm laser (0.5 W/cm^2) for 10 min, in comparison to the very modest temperature increase of free CD-GNPs or ADA-GNPs under the same conditions (Fig. 2I). The photothermal property of GNP aggregates was maintained after irradiation for 3 cycles (fig. S2B), making multiple photothermal treatments in vivo possible. In addition, as shown in fig. S2 (C and D), the largest size of aggregation was detected in the mixture of CD-GNPs and ADA-GNPs at a molar ratio of 1:1 in comparison to other molar ratios (10:1, 5:1, 1:5,

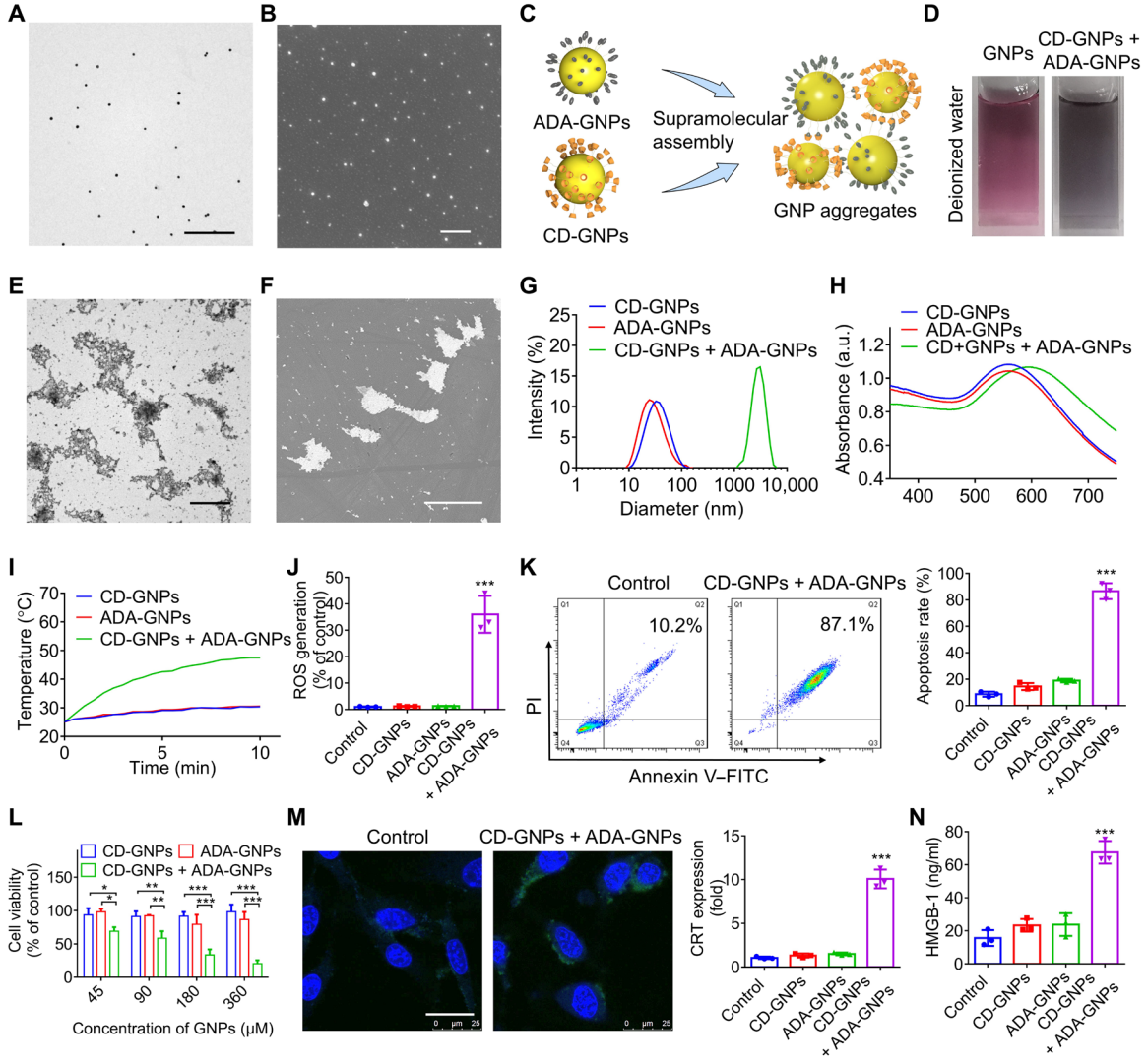

Fig. 2. Preparation of GNP aggregates and PTT-induced immunogenic tumor cell death. (**A**) TEM image of GNPs. Scale bar, 500 nm. (**B**) SEM image of GNPs. Scale bar, 500 nm. (**C**) Schematic illustration of the formation of GNP aggregates via supramolecular assembly between CD-GNPs and ADA-GNPs. (**D**) Photographs of GNP solution and mixture solution of CD-GNPs and ADA-GNPs. (**E**) TEM image of GNP aggregates. Scale bar, 2 μm. (**F**) SEM image of GNPs. Scale bar, 3 μm. (**G**) Size distribution of the mixture of CD-GNPs and ADA-GNPs determined by DLS. (**H**) Ultraviolet-visible (UV-vis) absorption spectra of CD-GNPs, ADA-GNPs, and the mixture of the two. a.u., arbitrary unit. (**I**) Photothermal curve of the mixture of CD-GNPs and ADA-GNPs (at a total concentration of 0.2 mg/ml of Au) under NIR irradiation with a laser of 808 nm (0.5 W/cm^2) for 10 min. (**J**) B16 cells were incubated for 6 hours after PTT treatment via GNP aggregates under an NIR laser for 10 min, and the DCF fluorescence was measured by flow cytometry to determine the ROS generation. (**K** and **L**) B16 cells were incubated for 24 hours after PTT treatment via GNP aggregates, the apoptosis rate was measured via flow cytometry (K), and cell viability was analyzed by MTT assays (L). (**M** and **N**) After incubation for 24 hours after PTT treatment, the CRT expression in B16 cells was imaged by CLSM and quantitatively analyzed by enzyme-linked immunosorbent assays (ELISAs) (M), and the released HMGB-1 in cell culture medium was quantified by ELISA assays (N). Scale bar, 25 μm. The experiments were repeated three times ($n = 3$) and data were presented as means ± SD. Statistical analysis for (I) was performed using two-way analysis of variance (ANOVA). All other analyses were conducted using one-way ANOVA. *$P \leq 0.05$, **$P \leq 0.01$, and ***$P \leq 0.001$.

and 1:10), and GNP aggregate from a molar ratio of 1:1 also exhibited the highest photothermal conversion efficiency (fig. S2E). Thus, mixture of CD-GNPs and ADA-GNPs at a GNP molar ratio of 1:1 was used to prepare GNP aggregates in this study.

The PTT treatment of B16 cells by GNP aggregates under NIR laser irradiation was further investigated. After incubation with the GNP aggregates for 3 hours, GNP aggregates were mostly observed outside B16 cells under confocal laser scanning microscopy (CLSM), expectedly due to their microscale sizes (fig. S3A). Subsequently, B16 cells were irradiated for 5 min with a laser of 808 nm (0.5 W/cm^2), the reactive oxygen species (ROS) production increased significantly after 6 hours (Fig. 2K and fig. S3B), and a high apoptosis rate (Fig. 2K and fig. S3C) and severe cell growth inhibition (Fig. 2L) were observed after incubation for additional 24 hours. ROS production is one of the essential components that govern intracellular ICD pathways and contributes to traffic DAMPs (damage-associated molecular patterns) to the extracellular space (*29*–*31*). The PTT effects of GNP aggregates could effectively induce ICD of B16 cells, as shown by calreticulin (CRT) cell surface exposure detected by CLSM and flow cytometry (Fig. 2M and fig. S4, A and B), increased

release of high-mobility group box-1 (HMGB-1; Fig. 2N) and adenosine triphosphate (ATP) production (fig. S4C) shown by enzyme-linked immunosorbent assays (ELISAs).

Intracellular supramolecular assembly of bacteria-mimetic GNPs

Considering the specific recognition and phagocytosis of bacteria by phagocytic immune cells (*32*–*34*), nonpathogenic OMVs of *E. coli* were coated onto GNPs via ultrasonic method to prepare the bacteria-mimetic GNPs, namely, M-GNPs. TEM showed that a transparent membrane layer with a thickness of 6 nm was coated on GNPs (Fig. 3A), and DLS showed an increased size from 30 to 45 nm after coating of GNPs with OMVs (Fig. 3B). In comparison with the black GNP solution, the color of M-GNPs remained pink in phosphate-buffered saline (PBS) solution (Fig. 3C). The diameter of OMV-coated GNPs increased in a very modest manner, even after storage for 1 month (fig. S5A), indicating a good stability of OMV coating, similar to a previous report (*35*). Furthermore, the absorption wavelength (Fig. 3D) and diameter (Fig. 3E) did not change after mixing M-CD-GNPs and M-ADA-GNPs. This result indicated that the OMV coating provided a protection layer to prevent supramolecular aggregation between CD-GNPs and ADA-GNPs, thereby making it possible for in vivo administration of the mixture of M-CD-GNPs and M-ADA-GNPs.

The protein bands of M-GNPs in the gel by Coomassie Blue staining were similar to those of OMVs (Fig. 3F), suggesting successful coating GNPs by OMVs (Fig. 3G). Mouse monocyte macrophage (RAW264.7 cells) and human normal liver cells (L-02 cells), respectively, selected as representative immune cells and nonimmune cells for in vitro study, were treated with cyanine5 (Cy5) NHS ester–labeled M-GNPs (M-Cy5-GNPs). After incubation for 3 hours, the fluorescence intensity of RAW264.7 cells treated with M-Cy5-GNPs was significantly increased, and the intracellular Au content was 2.5-fold as that in RAW264.7 cells treated with Cy5-GNPs (Fig. 3H). The internalized amount of Au in M-GNP–treated RAW264.7 cells was almost 10-fold as that in M-GNP–treated L-02 cells, indicating a highly selective phagocytosis of M-GNPs by immune cells. Furthermore, cytochalasin was used to inhibit macrophage pinocytosis. As shown in fig. S5B, the intracellular uptake of macrophage toward Cy5-labeled GNPs was significantly inhibited by cytochalasin, and the Au concentration in macrophage was decreased to 0.3098×10^{-3} ng per cell in comparison to 1.754×10^{-3} ng per cell from macrophage without cytochalasin treatment. Although cytochalasin treatment also reduced the intracellular Au concentration in macrophage treated with M-GNPs, the Au concentration remained a high level of 2.352×10^{-3} ng per cell and was much higher than that of macrophage treated with free GNPs and cytochalasin. The result further showed that OMV coating increased the internalization of macrophage toward GNPs. To investigate intracellular assembly process, the study of the degradation of coated OMVs in macrophages was first conducted, where OMVs were stained with DiO (green fluorescence) to prepare Mixture, and macrophage was stained with LysoTracker Red. As shown in fig. S6A, OMVs were quickly fused with macrophage membrane after incubation for 10 min and then distributed in red fluorescent lysosome at 30 min. After incubation for 60 min, the green fluorescence of OMVs nearly disappeared, suggesting the degradation of OMVs. To track the intracellular assembly process of Mixture in RAW264.7 cells, fluorescein isothiocyanate (FITC)–polyethylene glycol (PEG) (2k)-SH and Cy5-PEG (2k)-SH were conjugated onto ADA-GNPs and CD-GNPs, respectively, with PEG as a spacer to minimize the fluorescence quenching. As shown in Fig. 3I, the Cy5 fluorescence of M-CD-GNPs overlapped well with the FITC fluorescence of M-ADA-GNPs in RAW264.7 cells treated with the mixture of M-CD-GNPs and M-ADA-GNPs at an equal molar ratio of Au (Mixture) for 30 min, exhibiting a time-dependent manner, with the total Au content of 0.012 ng per cell after incubation for 9 hours (Fig. 3J). The TEM ultrastructure of RAW264.7 cells showed intracellular GNP aggregates with a mean diameter of 2 μm (Fig. 3K), confirming the intracellular self-assembly/aggregation of M-CD-GNPs and M-ADA-GNPs. Subsequently, in comparison with cells treated with M-CD-GNPs or M-ADA-GNPs alone, the Mixture-treated RAW264.7 cells remained a strong merged fluorescence intensity with a low efflux ratio (~32.5%) of GNPs after being placed in fresh media for 12 hours (Fig. 3L and fig. S6B), indicating that the formation of micrometer-sized GNP aggregates inhibited efflux of GNPs from macrophage.

The effect of GNP self-assembly/aggregation on macrophage function

The effect of intracellular GNP self-assembly/aggregation on the physiological function of RAW264.7 cells was further investigated. Figure 4 (A and B) showed that intracellular GNP aggregates had negligible cytotoxicity to RAW264.7 cells even at a high concentration of 200 μM Au, and nearly all cells were alive after incubation for 24 hours. As shown in Fig. 4C, RAW264.7 cells were plated on the upside of the insert, and melanoma (B16) cells were seeded in the bottom of chamber. In comparison to that of free RAW264.7 cells, the intracellular self-assembly of GNPs had negligible effects on the migration ability (Fig. 4, D and E) and invasion ability of RAW264.7 cells through matrix (Fig. 4, F and G). Moreover, the FITC fluorescence of M-ADA-GNPs overlapped with the Cy5 fluorescence of M-CD-GNPs inside the RAW264.7 cells (Fig. 4F), indicating that RAW264.7 cells went through the matrix with the intracellular GNP aggregates. Furthermore, M-CD-GNPs and M-ADA-GNPs, respectively, induced the production of tumor necrosis factor–α (TNF-α) and interleukin-1β (IL-1β; Fig. 4H) and M1 polarization (Fig. 4I) of RAW264.7 cells, attributed to the lipopolysaccharide (LPS) in the OMV coating [LPS (6.08 μg/ml) in M-GNPs (2 mg/ml)]. However, when the cells were incubated with Mixture at the same dose of GNPs, the inflammatory factors reached a high level and the percentage of M1 macrophage further increased to 68.5%, indicating that large size of intracellular GNP aggregates and OMVs synergistically induced M1 polarization and promoted secretion of inflammatory cytokines, whereas no negative influence on the physiological function of RAW264.7 cells was exhibited.

Immune cell–hitchhiking delivery of GNP aggregates to the tumor

Six-week-old male mice were subcutaneously inoculated with B16 cells and randomly and blindly divided into three groups ($n = 3$) to investigate in vivo hitchhiking of immune cells and increased hitchhiking delivery to the tumor tissues. After administration with Cy5-modified free GNPs (Cy5-GNPs), Cy5-modified M-GNPs (M-Cy5-GNPs), and the mixture of Cy5-labeled M-CD-GNPs and M-ADA-GNPs at a molar ratio of 1:1 (Cy5-Mixture) at the Cy5 dose of 0.5 mg/kg for 1 hour, respectively, the Au contents in phagocytic immune cells of mice treated with Mixture or M-GNPs reached a high level (~85 μg per immune cell), when compared with

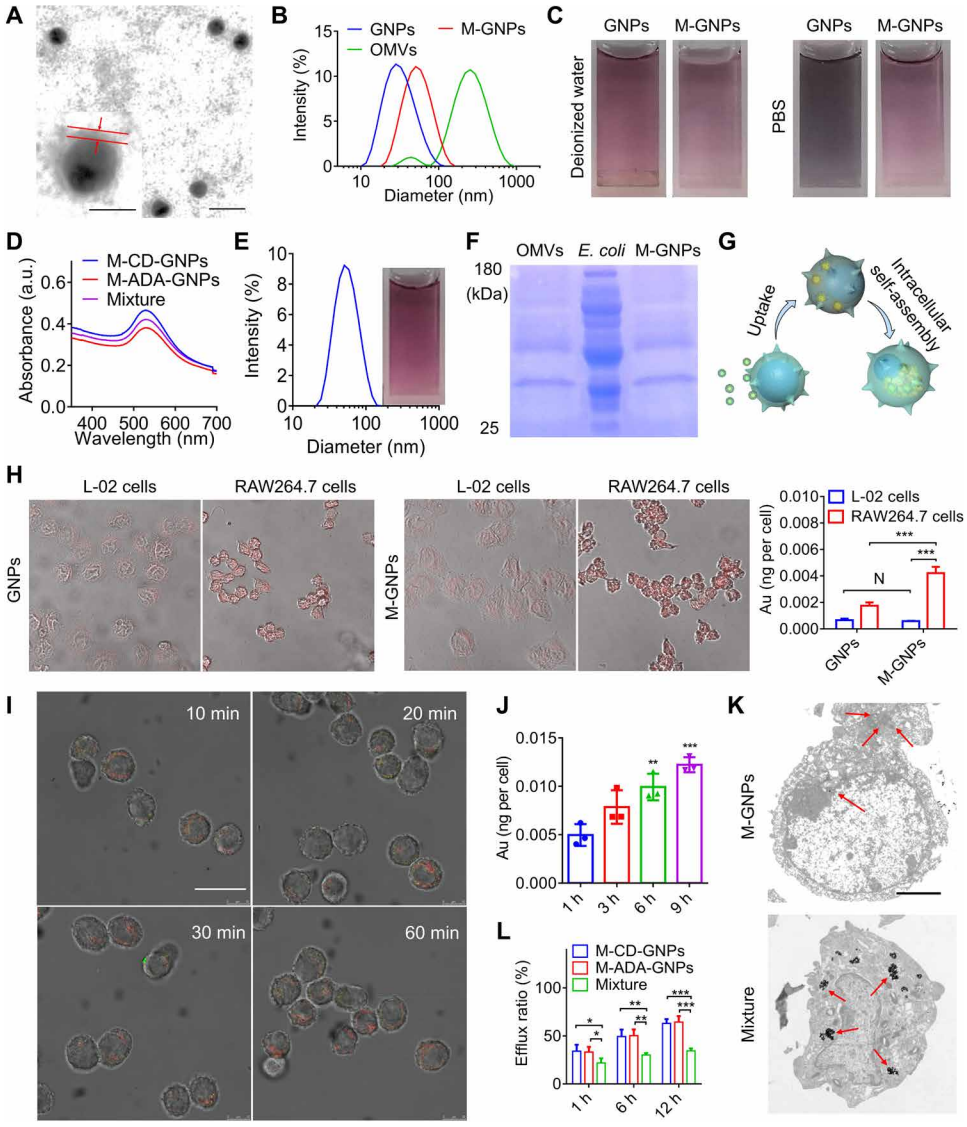

Fig. 3. Selective phagocytosis and intracellular self-assembly of M-GNPs in macrophage. (**A**) TEM image of M-GNPs. Scale bar, 50 nm. Insert: Amplified M-GNPs (scale bar, 20 nm). (**B**) Size distribution of GNPs, M-GNPs, and OMVs. (**C**) Photographs of GNPs and M-GNPs in deionized water or PBS. (**D**) UV-vis absorption spectrum of Mixture. (**E**) Size distribution and photograph of Mixture. (**F**) The protein bands of M-GNPs, OMVs, and *E. coli* in the gel by Coomassie Blue staining. (**G**) Scheme showing selective intracellular uptake and self-assembly of M-GNP Mixture. (**H**) Fluorescence imaging on the intracellular uptake of GNPs and M-GNPs by L-02 cells and RAW264.7 cells, respectively, and the quantitative analysis on the intracellular Au content by ICP-MS. (**I**) RAW264.7 cells were incubated with the mixture of M– fluorescein isothiocyanate (FITC)–ADA-GNPs and M-Cy5-CD-GNPs for different durations (10, 20, 30, and 60 min), and CLSM imaging was conducted at 9 hours. Scale bar, 20 μm. (**J**) Intracellular Au content in RAW264.7 cells was analyzed via ICP-MS, after incubation with the mixture of M-FITC-ADA-GNPs and M-Cy5-CD-GNPs for 3, 6, and 9 hours. (**K**) TEM imaging on Mixture- and M-GNP–treated RAW264.7 cells, respectively. Scale bar, 2.5 μm. (**L**) After treatment with the mixture of M-FITC-ADA-GNPs and M-Cy5-CD-GNPs for 6 hours, RAW264.7 cells were incubated in fresh media for different durations (1, 6, and 12 hours) and quantified by ICP-MS at all preset time points. The experiments were repeated three times ($n = 3$) and data were presented as means ± SD. Statistical analysis for (I) and (L) were performed using two-way ANOVA. All other analyses were conducted using one-way ANOVA. $^{*}P \leq 0.05$, $^{**}P \leq 0.01$, and $^{***}P \leq 0.001$.

that of the GNP-treated group (~25 μg per immune cell), indicating that bacteria-mimetic strategy enhanced in vivo uptake of M-GNPs by immune cells (Fig. 5A). After administration for 24 hours, the intracellular Au content in immune cells of M-GNP–treated mice decreased significantly, in contrast to the high Au content in immune cells of Mixture-treated group (~50 μg per immune cell), which was further confirmed by the flow cytometry analysis of Cy5 fluorescence intensity in immune cells (fig. S7A), $CD11b^{+}$ cells, and $CD11c^{+}$ cells (Fig. 5B and fig. S7B). Furthermore, circulating neutrophils and monocytes in the blood were identified as $Ly\text{-}6G^{+}$ cells and $CD11b^{+}CD115^{+}$ cells, respectively. Figure S7 (C to F) showed that neutrophils and monocytes from Mixture-treated group had high Au content intracellularly, which were 1.49- and 1.56-fold that of M-GNP–treated mice and 3.18- and 3.91-fold that of GNP-treated mice, respectively. These results suggest that the large size of supramolecular GNP aggregates (mediated via supramolecular self-assembly intracellularly) significantly inhibited the efflux effect of immune cells, and Mixture was mainly phagocytosed by the circulating immune

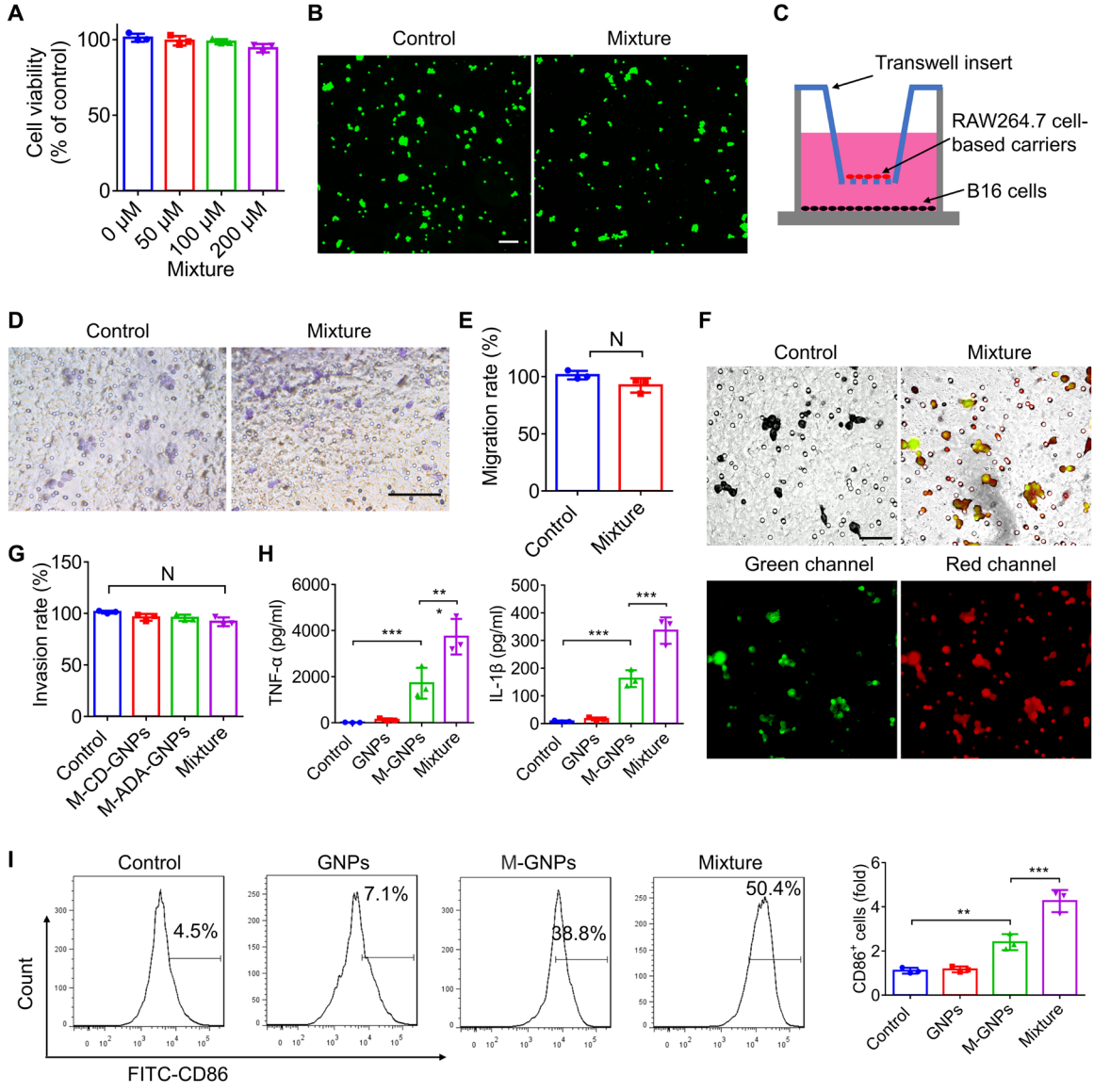

Fig. 4. The effects of intracellular self-assembly of GNPs on macrophage. (**A**) Viability of RAW264.7 cells incubated with different concentrations of Mixture for 24 hours (the total concentration of Au of 50, 100, and 200 μM). (**B**) Live/dead cell staining on RAW264.7 cells after treatment with 200 μM Mixture (the total concentration of Au). Scale bar, 100 μm. (**C**) Scheme showing the migration and invasion test of macrophage. (**D** and **E**) RAW264.7 cells were incubated with Mixture at a total Au of 0.2 mg/ml for 6 hours, and the migrated cells toward B16 cells were photographed (D) and quantified (E) after incubation for additional 24 hours. Scale bar, 100 μm. N, no statistical significance. (**F** and **G**) Fluorescence imaging (F) and quantitative analysis (G) of RAW264.7 cells that went through the matrix with intracellular GNP aggregates (FITC-labeled ADA-GNPs and Cy5-labeled CD-GNPs) at a total concentration of 0.2 mg/ml of Au. Scale bar, 50 μm. (**H** and **I**) The level of TNF-α and IL-1β (H) in the cell culture medium and M1 polarization (I) of RAW264.7 cells were determined by ELISA assay and flow cytometry respectively, after treatment with Mixture at a total concentration of 0.2 mg/ml of Au for 24 hours. The experiments were repeated three times ($n = 3$) and data were presented as means ± SD. All statistical analysis was performed using one-way ANOVA. *$P \leq 0.05$, **$P \leq 0.01$, and ***$P \leq 0.001$.

cells (neutrophils or monocytes) in the blood. Pharmacokinetic analysis on the fate of Mixture was conducted by measuring the change of blood Cy5 fluorescence intensity at different time points for up to 24 hours (Fig. 5C). Figure 5D showed that the half-life ($T_{1/2}$) of M-Cy5-GNPs was 2.8 hours, lower than Cy5-GNPs with $T_{1/2}$ of 3.8 hours, attributed to the quick phagocytosis and clearance of nanosized GNPs (~20 nm) by phagocytic immune cells (*36*–*38*). In contrast, the $T_{1/2}$ of Mixture was extended to 9.2 hours, exhibiting a long circulation time due to the formation of intracellular GNP aggregates that significantly retarded the exocytosis, thereby slowing down the clearance by mononuclear phagocyte system (*39*, *40*).

After verifying the in vivo construction of immune cell–based carriers, the biodistribution of Mixture in B16 tumor–bearing mouse was investigated via an in vivo imaging system (IVIS) at preset time points (up to 24 hours; Fig. 5E). In comparison with that of mice treated with Cy5-GNPs, bright red fluorescence was observed in the tumor sites of both mice treated with M-Cy5-GNPs and Mixture in the first few hours after administration, resulting from the enhanced intracellular uptake and immune cell–hitchhiking delivery of

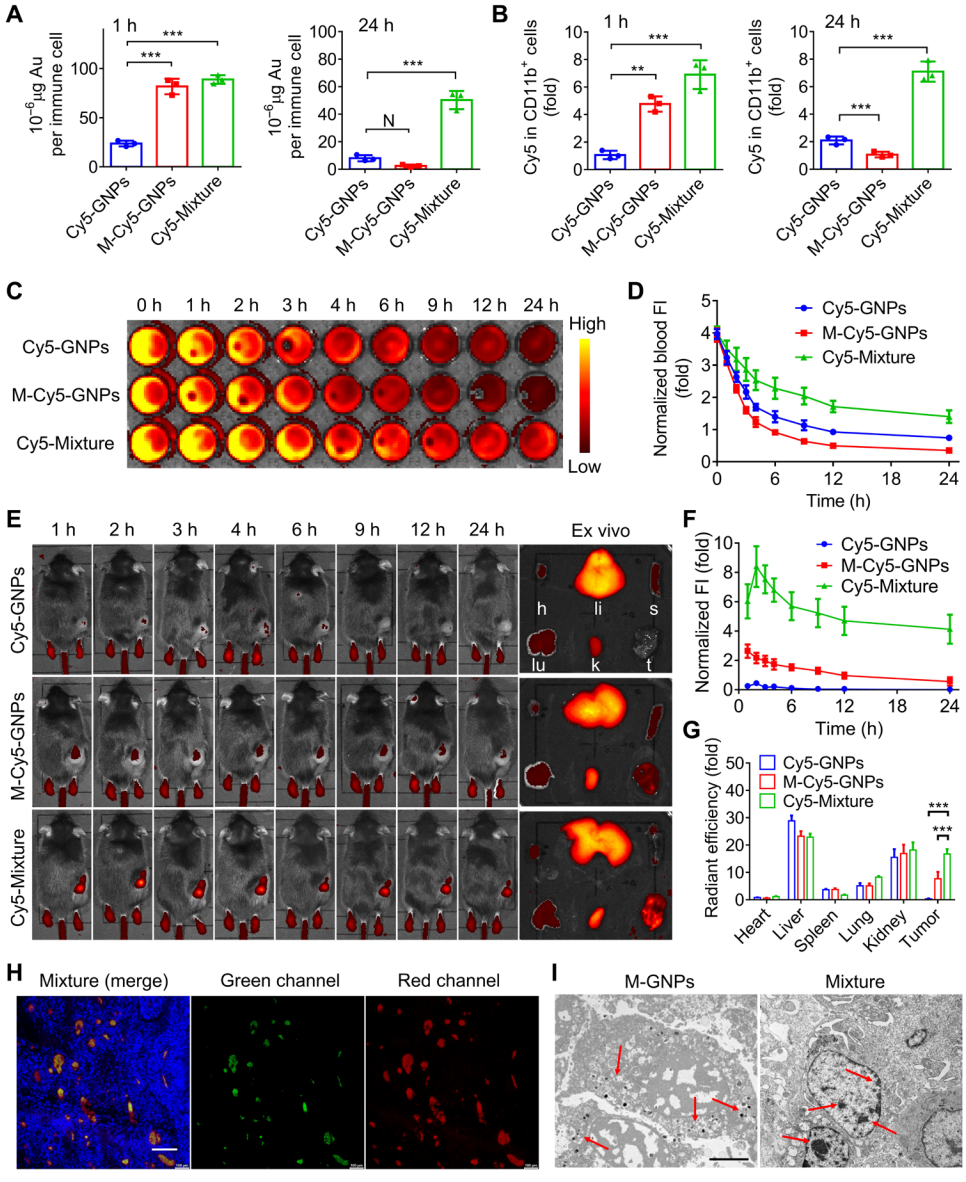

Fig. 5. In vivo construction of immune cell–based nanomedicine carriers and increased hitchhiking delivery to the tumors. (**A** and **B**) Melanoma mice were treated with Cy5-GNPs, M-Cy5-GNPs, and Cy5-Mixture at the Cy5 dose of 0.5 mg/kg for 24 hours, and the quantitative analysis of Au content (A) and Cy5 fluorescence (B) was conducted in the collected immune cells at 1 and 24 hours after administration, by using ICP-MS and flow cytometry, respectively. h, hour or hours. (**C** and **D**) Fluorescence imaging of the blood (C) collected from Cy5-Mixture–treated mice at different time points (1, 2, 3, 4, 6, 9, 12, and 24 hours) and the corresponding fluorescence intensity (FI)–time curves (D). (**E** to **G**) In vivo fluorescence images (E) and intensity-time curves (F) of Cy5-Mixture–treated mice at different time points (1, 2, 3, 4, 6, 9, 12, and 24 hours) and ex vivo imaging (E) and quantified radiant efficiency (G) on the heart (h), liver (li), spleen (s), lung (lu), kidney (k), and tumor (t) collected from melanoma mice after administration for 24 hours. (**H**) Fluorescent section analysis on the tumor collected from mice treated with the mixture of FITC-labeled M-ADA-GNPs and Cy5-labeled M-CD-GNPs for 24 hours. Green, FITC-labeled ADA-GNPs; red: Cy5-labeled CD-GNPs. Scale bar, 200 μm. (**I**) TEM analysis of GNP aggregates and GNPs in the collected tumor tissues after administration for 24 hours. Scale bar, 3 μm. The experiments were repeated three times ($n = 3$) and data were presented as means ± SD. Statistical analysis for (G) was performed using two-way ANOVA. All other analyses were conducted using one-way ANOVA. $^{**}P \leq 0.01$ and $^{***}P \leq 0.001$.

M-Cy5-GNPs to the tumor site. After administration for 12 hours, the fluorescence signal decreased quickly in the tumor of M-Cy5-GNP–treated mice, whereas the tumor of mice treated with Mixture maintained a strong and sustainable red fluorescence signal (Fig. 5F). The ex vivo fluorescence imaging further confirmed the long retention time of micrometer-sized GNP aggregates in the tumor tissues of mice treated with Mixture, and the tumor fluorescence intensity increased to 50.7-fold that of mice treated with free GNPs and 2.17-fold that of mice treated with M-GNPs, after administration for 24 hours (Fig. 5, E and G). Moreover, a large area of strong fluorescence was detected in section analysis of the tumor collected from mice treated with the mixture of FITC-labeled M-ADA-GNPs and Cy5-labeled M-CD-GNPs for 24 hours, and the fluorescence of Cy5 overlapped well with FITC, indicating the accumulation of GNP aggregates in the tumor (Fig. 5H). In contrast, only weak fluorescence signal with high dispersion was observed in M-Cy5-GNP– or

Cy5-GNP–treated group of mice (fig. S7G). TEM imaging of the tumor tissues directly showed GNP aggregates with a diameter of ~1.2 μm in Mixture-treated mice, in contrast to small dark GNP dots (~30 nm) observed in the M-GNP–treated mice (Fig. 5I). These results indicated the successful in vivo hitchhiking of immune cells by bacteria-mimetic GNPs and the increased hitchhiking delivery of GNP aggregates to the tumor tissues, which inhibited the efflux from immune cell–based carriers and prolonged their retention time in the tumor tissues.

Initial PTT enhanced recruitment of immune cell–based carriers

After intravenous infusion of GNPs, M-GNPs, and Mixture at GNPs (10 mg/kg) into mice for 1 hour, the tumor sites were externally irradiated by NIR (808 nm) at 0.5 W/cm^2 power. As expected, the photothermal effects were only detected in the Mixture-treated mice due to the accumulation of GNP aggregates, and the temperature in the tumor site increased to 55°C after irradiation for only 5 min (fig. S8). Subsequently, in accordance with the in vivo biodistribution of these materials (Fig. 5, E and F), photothermal imaging was conducted at the same preset time points in mice. As shown in Fig. 6A, an obviously high temperature was recorded in Mixture-treated mice at all time points. As the photothermal efficiency has a positive correlation with the dose of GNP aggregates (fluorescence intensity of GNP aggregation) in the tumor tissues, it was unexpected to find that the trend of temperature curve was not positively correlated with the in vivo biodistribution curve of Mixture in mice (Figs. 5F and 6B). The largest fluorescence intensity of GNP aggregation was observed at 2 hours after administration, but the highest temperature was observed at 4 hours after administration.

To explain this observation, the tumor was collected after NIR irradiation at 1 hour after administration. As shown in Fig. 5C, in comparison with the black tumor tissues isolated from GNP-treated mice and M-GNP–treated mice, the tumor from Mixture-treated mice showed certain pale white area (Fig. 6C), likely attributed to the high-temperature–induced tissue damage. Furthermore, the inflammatory cytokines (TNF-α and IL-1β) in the tumor tissue of Mixture-treated mice also increased significantly (Fig. 6D). After initial NIR irradiation at 1 hour after administration, the TNF-α concentration in the tumor tissue of Mixture-treated mice maintained a high level at different time points and reached highest concentration at 4 hours after administration, in contrast to that of the Mixture-treated mice without NIR irradiation (Fig. 6E). These results showed that an initial PTT treatment at 1 hour after administration induced tumor damage and increased the production of inflammatory cytokines, which may provide positive feedback to recruit more immune cells to the tumor tissues. Thus, the in vivo biodistribution of Mixture was further investigated with an initial PTT treatment at 1 hour after administration. As shown in Fig. 6 (F and G), the red fluorescence signal of Cy5 in the tumor tissues reached the highest intensity at 4 hour after administration, consistent with the trend of TNF-α concentration over time, indicating an enhanced accumulation of GNP aggregates after an initial PTT. In comparison with the biodistribution of Mixture in mice (Fig. 5F), the fluorescence intensity in the tumor tissues with an initial PTT treatment at 1 hour was much stronger and maintained a high level (Fig. 6G) for the following hours. Ex vivo fluorescence imaging of mice after administration for 24 hours showed that an initial PTT treatment increased the fluorescence intensity (from GNP aggregates) in the tumor tissues to 1.78-fold that of mice without PTT treatment (Fig. 6, H and I), indicating that the initial PTT treatment increased the tumor recruitment of immune cells and significantly improved targeted hitchhiking delivery of GNP aggregates by immune cells.

Inhibition of tumor growth by bacteria-mimetic GNP Mixture

Subsequently, the antitumor efficacy of Mixture was assessed with two NIR laser irradiations (5 min each time) sequentially conducted at 1 and 4 hours, respectively, after administration. An immune check point blockage agent [atezolizumab, anti-programmed death-ligand 1 (aPD-L1)] was selected for synergistically assisting the antitumor immunotherapy induced by PTT treatments. However, after treatment with 8 μg of aPD-L1 per mouse every 3 days for five doses in total, aPD-L1 exhibited little inhibition effects on the growth of melanoma tissue (fig. S9A), which was consistent with our previous study (*41*). In this investigation, the melanoma mice were randomly and blindly separated into five groups, followed by intravenous administration with PBS, M-GNPs with NIR irradiation at 1 hour after administration [M-GNPs (1 hour)], Mixture with NIR irradiation at 1 hour after administration [Mixture (1 hour)], Mixture with NIR irradiations at 1 and 4 hours, respectively [Mixture (1 and 4 hours)], and Mixture (1 and 4 hours) assisted by 8 μg of aPD-L1 per mouse every 3 days for five doses in total [Mixture (1 and 4 hours) + aPD-L1], at the same GNP dose of 10 mg/kg (Fig. 7A). As shown in Fig. 7B, the Mixture (1 hour) treatment delayed the growth of tumor and extended the overall survival time of melanoma mice, but all mice still died at the end of the experiment. In contrast, Mixture (1 and 4 hours) effectively decreased the tumor size and increased the survival rate to 50% by the end of the experiment, and more significantly, all mice survived with the assistance of aPD-L1, attributed to the PTT-induced ICD of B16 cells and the activated antitumor immunity. After administration for 7 days, the tumor tissues were collected from another batch of melanoma mice in a parallel experiment, the tumor photos further showed the effective antitumor effect of Mixture (1 and 4 hours) + aPD-L1 (Fig. 7C). Furthermore, the lung metastasis of B16 cells was obviously inhibited and there were no metastatic nodules observed in mice treated with Mixture (1 hour), Mixture (1 and 4 hours), or Mixture (1 and 4 hours) + aPD-L1(Fig. 7D). Moreover, the hematoxylin and eosin (H&E) staining, terminal deoxynucleotidyl transferase–mediated deoxyuridine triphosphate nick end labeling (TUNEL) staining, and caspase-3 staining of the tumor sections confirmed that Mixture (1 and 4 hours) effectively induced tumor necrosis and apoptosis, in comparison to Mixture (1 hour), which was further strengthened by aPD-L1 (Fig. 7E).

Mechanism of antitumor immunotherapy assisted by aPD-L1

As an initial immune response involved in the process of immune development (*42*, *43*), the antigen-presenting innate immune cells in the tumors collected on day 7 were investigated first. The increased tumor infiltration of F4/80$^+$ cells (Fig. 8A and fig. S10) and CD11c$^+$ cells (Fig. 8B and fig. S11) after treatment of mice by Mixture (1 hour) was observed, and two sequential PTT treatments [Mixture (1 and 4 hours)] exhibited a much higher intratumoral level of antigen-presenting immune cells. The main function of macrophages is to digest the dead tumor cells and secret proinflammatory cytokines to recruit other immune cells and to present the antigens to dendritic cells (DCs), while DCs could process antigens before presenting them to T cells, which strengthens immunity response (*44*, *45*). The enhanced intratumoral infiltration of macrophages and DCs should

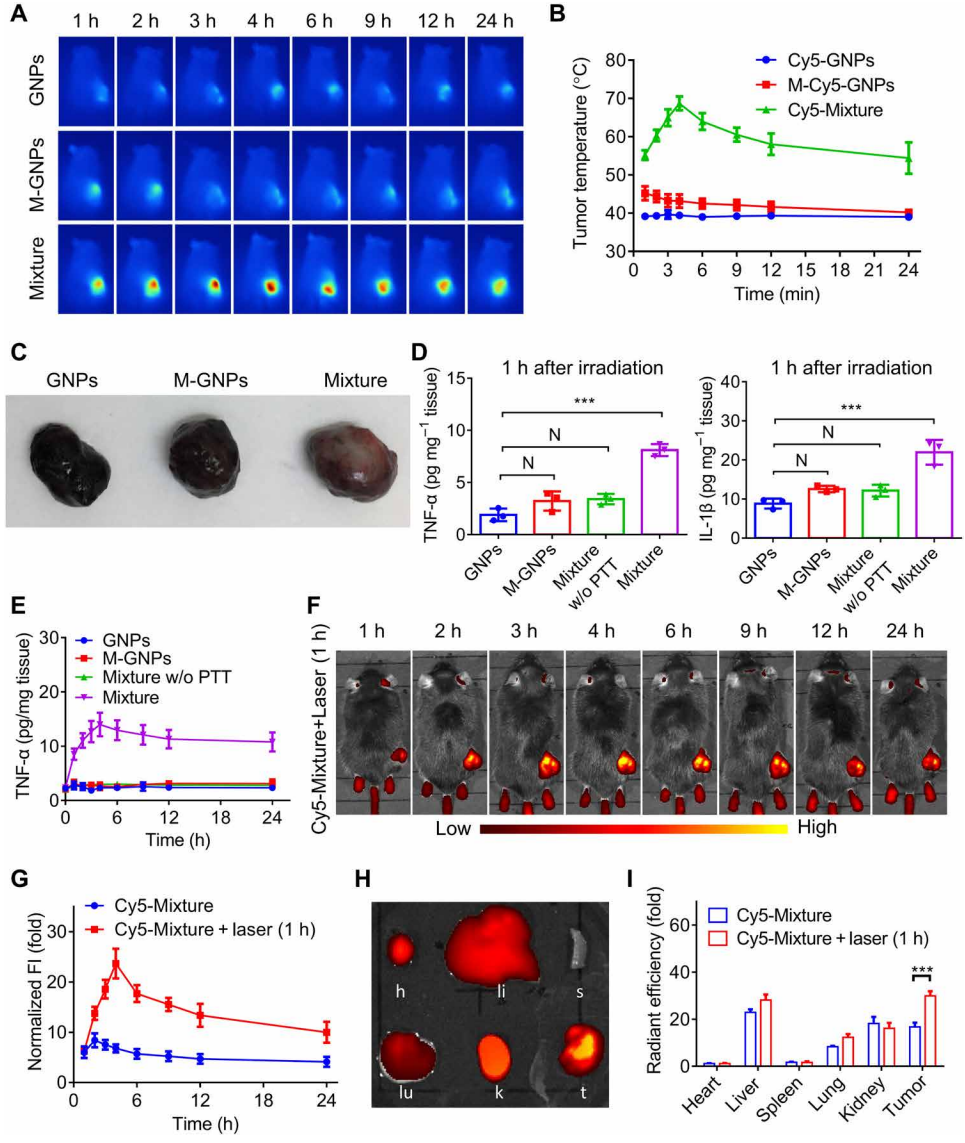

Fig. 6. Initial PTT treatment enhanced tumor inflammation and recruitment of immune cell–based nanomedicine carriers, leading to significant tumor accumulation of GNP aggregates. (**A** and **B**) After intravenous administration of GNPs, M-GNPs, and Mixture at a GNP dose of 10 mg/kg into melanoma-bearing mice for different durations (1, 2, 3, 4, 6, 9, 12, and 24 hours), photothermal imaging was conducted on melanoma mice under NIR irradiation (808 nm) for 5 min at a power of 0.5 W/cm^2 (A), and the temperature in the tumor sites was recorded (B). (**C** and **D**) After NIR irradiation for 5 min at 1 hour after administration, the tumor tissues (C) were collected from mice treated with GNPs, M-GNPs, and Mixture, the Mixture-treated mice without NIR irradiation served as a control group, and the level of TNF-α and IL-1β (D) in the tumors was quantified via ELISA assays. (**E**) After the initial PTT treatment at 1 hour after administration, the TNF-α concentration in the tumor of Mixture-treated mice was measured at different time points. (**F** and **G**) In vivo fluorescence imaging (F) and quantitative analysis of fluorescence intensity in the tumors (G) were conducted in mice after administration with Mixture for different times. (**H** and **I**) Ex vivo fluorescence imaging (H) and quantitative analysis (I) of fluorescence intensity of the heart (h), liver (li), spleen (s), lung (lu), kidney (k), and tumor (t) were analyzed in Mixture-treated mice at 24 hours after administration. The experiments were repeated three times ($n = 3$) and data were presented as means ± SD. Statistical analysis for (I) was performed using two-way ANOVA. All other analyses were conducted using one-way ANOVA. ***$P \leq 0.001$.

be attributed to the enhanced immunogenicity caused by Mixture and PTT treatment, which has been verified on the PTT-induced ICD of B16 cells (Fig. 2, D to G). In comparison with Mixture (1 and 4 hours) and free aPD-L1 (fig. S9, B to I), flow cytometry analysis (Fig. 8, C and D, and figs. S12 and S13) showed the increased M1 macrophages (F4/80$^+$CD11b$^+$CD86$^+$ cells) and DCs (CD45$^+$CD11b$^+$ CD11c$^+$ cells) in the tumors of mice treated with Mixture (1 and 4 hours) + aPD-L1, suggesting that the combination therapy enhanced the polarization of M1 macrophages and recruited more DCs to the tumor tissues to facilitate antigen presentation to T cells. Immunofluorescence analysis exhibited modest increase in the infiltration density of CD3$^+$CD8$^+$ cells in the tumor after the initial PTT treatment of Mixture (1 hour), and the two sequential PTT treatments [Mixture (1 and 4 hours)] exhibited a much higher intratumoral level of these cells (Fig. 8E), providing direct evidence for PTT-induced tumor microenvironment changes by increasing the quantity

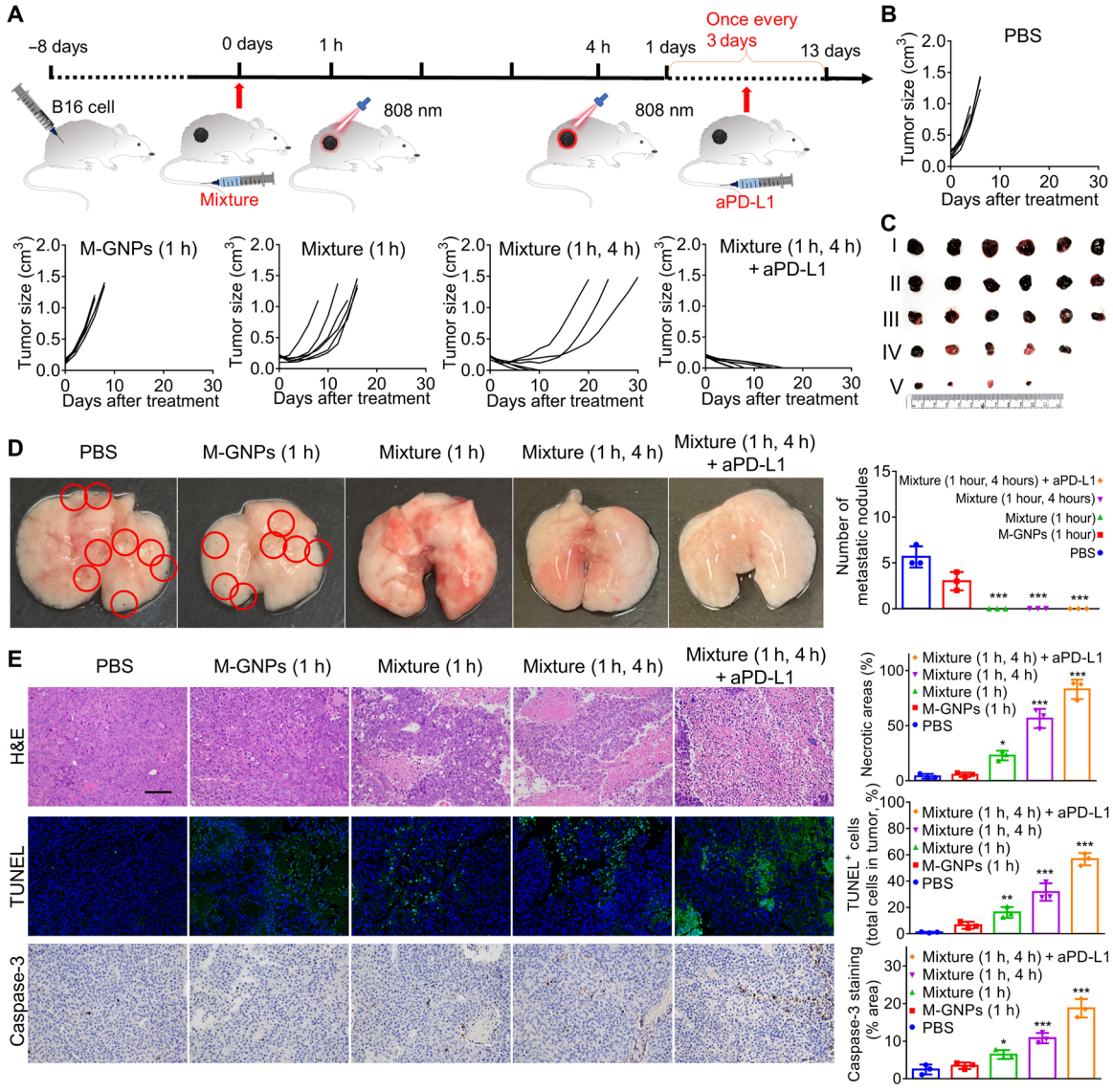

Fig. 7. Improved antitumor efficacy of Mixture via two PTT treatments (1 and 4 hours), assisted by aPD-L1. (**A**) Schematic illustration of antitumor experiment in mice by Mixture with two NIR laser irradiations (808 nm for 5 min each time) at 1 and 4 hours, respectively, after administration, assisted by immune checkpoint blockage. (**B**) The change of tumor volume in mice treated with PBS, M-GNPs (1 hour), Mixture (1 hour), Mixture (1 and 4 hours), and Mixture (1 and 4 hours) + aPD-L1 at a GNP dose of 10 mg/kg and 8 μg of aPD-L1 per mouse every 3 days for five doses in total ($n = 6$). (**C**) Photographs of the tumor tissues collected on day 7. I: PBS. II: M-GNPs (1 hour). III: Mixture (1 hour). VI: Mixture (1 and 4 hours). V: Mixture (1 and 4 hours) + aPD-L1. (**D**) Photographs of the lung tissues collected on day 7 and quantitative analysis on metastatic nodules. (**E**) H&E staining, TUNEL staining, and caspase-3 staining of the tumor tissues collected on day 7. Scale bar, 100 μm. The experiments for (C), (D), and (E) were repeated three times ($n = 3$) and data were presented as means ± SD. All statistical analyses were performed using one-way ANOVA. $^{*}P \leq 0.05$, $^{**}P \leq 0.01$, and $^{***}P \leq 0.001$.

of cytotoxic T cells. Flow cytometry analysis also confirmed that Mixture (1 and 4 hours) increased the number of $CD3^{+}CD8^{+}$ T cells and $CD3^{+}CD4^{+}$ T cells in the tumors (Fig. 8F and fig. S14), which was further increased upon addition of aPD-L1. These results demonstrated that Mixture (1 and 4 hours), with two PTT treatments, effectively increased tumor accumulation of GNP aggregates via in vivo hitchhiking immune cells, leading to significantly enhanced PTT treatment–induced change of the tumor microenvironment, and tumor-specific T cell response to potentiate checkpoint blockade immunotherapy (aPD-L1) against melanoma.

In vivo safety evaluation

As potential reactogenicity to endotoxin remains one of the main concerns for the safe use of OMVs (*46*, *47*), mice were intravenously administered with 1- and 10-fold Mixture, respectively, of that used in the antitumor experiment, for safety evaluation. After administration for 1 hour, the level of TNF-α and IL-6 in the serum (fig. S15, A and B) increased and the number of white blood cells (fig. S15C) decreased in 10× Mixture–treated mice, whereas nearly negligible change was observed in 1× Mixture–treated mice. After administration for 24 hours, all these parameters of both groups of mice returned

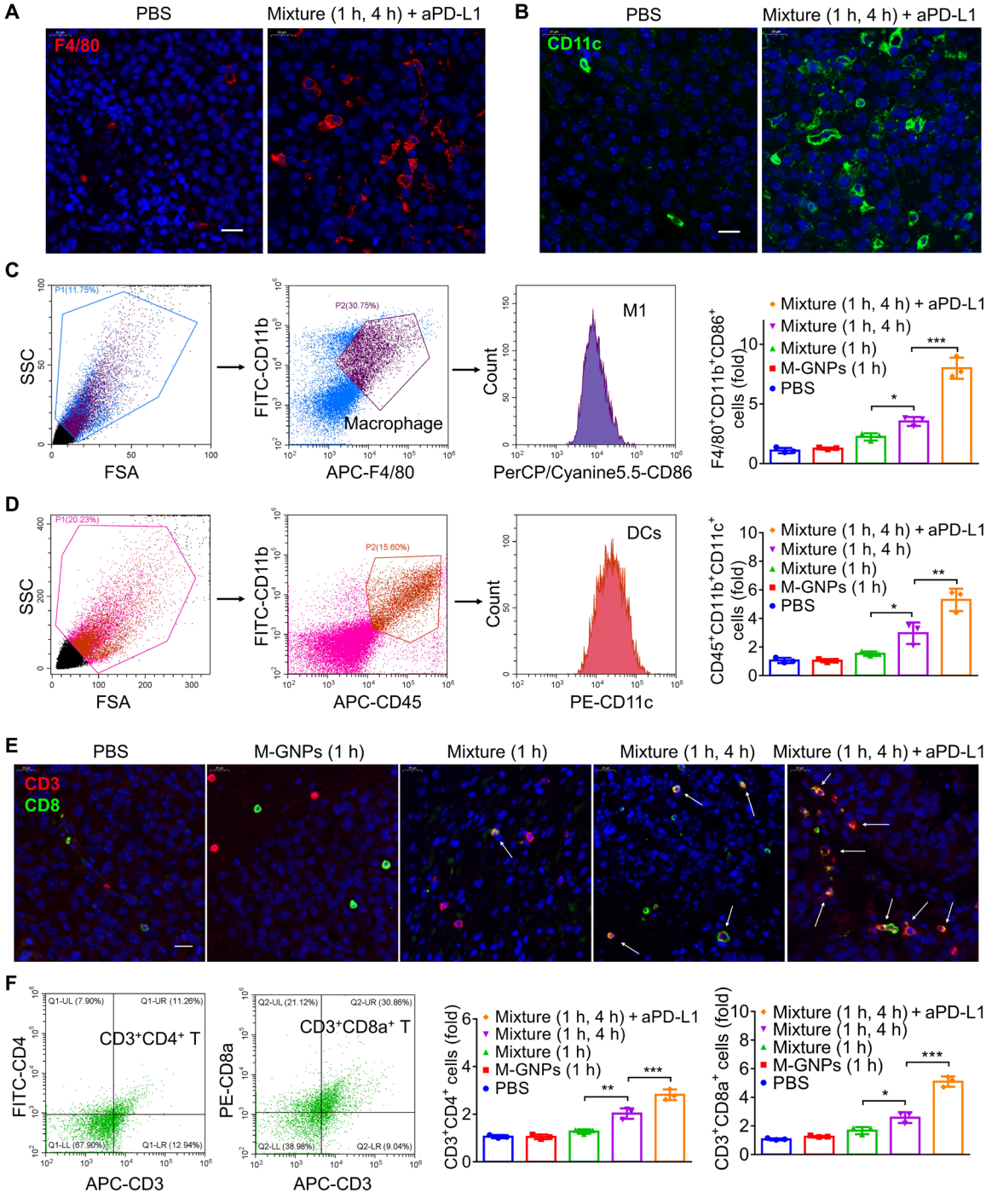

Fig. 8. Enhanced intratumoral infiltration of immune cells by PTT treatment induced ICD with or without aPD-L1. (**A** and **B**) Immunofluorescence analysis on the infiltration of F4/80$^+$ cells (A) and CD11c$^+$ cells (B) in the tumor tissues collected from mice after administration for 7 days. (**C** and **D**) Flow cytometry analysis on M1 macrophages (F4/80$^+$CD11b$^+$CD86$^+$ cells) (C) and DCs (CD45$^+$CD11b$^+$CD11c$^+$ cells) (D) in the tumor tissues collected on day 7. (**E**) Immunofluorescence analysis on the infiltration of CD3$^+$CD8$^+$ cells into the tumor tissues collected from mice after administration for 7 days. (**F**) Flow cytometry analysis of CD4$^+$ T cells (CD3$^+$CD4$^+$ cells) and CD8$^+$ T cells (CD3$^+$CD8a$^+$ cells) in the tumor tissues collected on day 7. The experiments were repeated three times ($n = 3$) and data were presented as means ± SD. All statistical analyses were performed using one-way ANOVA. *$P \leq 0.05$, **$P \leq 0.01$, and ***$P \leq 0.001$.

to the normal levels comparable to those of mice in the control group, and the H&E staining on the liver, spleen, lungs, and kidneys showed negligible damage (fig. S15D), which was further confirmed by the analysis of hepatic function biomarkers including alanine transaminase (ALT) and aspartate transaminase (AST; fig. S15E) and renal function biomarkers including urea nitrogen (BUN) and uric acid (UA; fig. S15F). Moreover, to evaluate the possible polarization of immune cells in the blood after administration with

Mixture and 10× Mixture for 24 hours, measurement of toll-like receptor (TLR) signaling on the circulating leukocytes was conducted. As shown in fig. S16 (A to D), the percent of Ly-6G$^+$TLR4$^+$ cells and CD11b$^+$CD115$^+$TLR4$^+$ cells in Mixture-treated mice returned to the normal levels comparable to those of the control group, and the polarization of leukocyte in 10× Mixture–treated mice was only modestly increased. The results showed that 10× Mixture induced very modest acute inflammation and the symptoms were quickly alleviated, whereas negligible systemic toxicity was observed in 1× Mixture–treated mice in this investigation.

In addition, safety evaluation was also conducted in mice treated with Mixture followed by an initial PTT treatment and a secondary PTT treatment. As shown in fig. S17 (A and B), after both the initial PTT treatment and the secondary PTT treatment for 3 hours, the level of TNF-α and IL-6 in the serum of Mixture-treated mice increased, and the number of white blood cells decreased. However, negligible damage was observed in the liver, spleen, kidneys, and lungs (fig. S17, C to E). The result showed that the initial PTT and the secondary PTT in Mixture-treated mice would induce modest systemic inflammation; however, no off-target damages on the spleen, liver, kidneys, and lungs were observed.

To overcome the current challenges faced by in vitro construction of cell-based nanomedicine carriers and to inhibit the efflux of nanomedicine from cells, this study came up an in vivo construction strategy of cell-based nanomedicine carriers for increased hitchhiking delivery, via selective phagocytosis of bacteria-mimetic nanomedicine and subsequent supramolecular aggregation inside phagocytic immune cells via host-guest chemistry–mediated self-assembly. Different nanomedicine coating or biomimicry could be designed for degradation in response to different intracellular environment and stimuli, such as pH, GSH, ATM, and enzymes. As different cells have different physiological functions, the responsiveness of the nanomedicine's coating material could be specifically designed according to the required type of cells as carriers for targeted delivery, such as platelets, stem cells, red blood cells, macrophages, T cells, or even tumor cells.

Notably, in vivo safety evaluation showed that 10× Mixture induced very modest acute inflammation, and the symptoms were quickly alleviated, whereas negligible systemic toxicity was observed in 1× Mixture–treated mice in this investigation. The aim of OMV coating on GNPs was to induce intracellular uptake by the circulating immune cells; therefore, a relevant low dose of OMVs would do. The dose of OMVs could be controlled as one of the quality control attributes when this technology is applied in large animal models or future clinical studies. In principle, liposomes modified with specific antibody to recognize immune cells may replace OMVs to induce selective phagocytosis by immune cells in vivo, as a feasible in vivo cell-hitchhiking strategy to further improve the safety.

In the study of immune cell–hitchhiking delivery of supramolecular GNP aggregates to the tumor tissues, we found that the initial PTT treatment caused tumor damage and increased the inflammatory signal from the tumor tissue, leading to enhanced recruitment of immune cells (including cell-based carriers) with a positive feedback. The optimized dual PTT treatments on melanoma mice administered with Mixture (1 and 4 hours) exhibited significantly improved intratumoral infiltration of M1 macrophage, DCs, CD4$^+$, and CD8$^+$ T cells, potentiating checkpoint blockade immunotherapy (aPD-L1) against melanoma. The positive feedback induced by the initial PTT treatment could be extended to other therapeutic modalities, such as chemotherapy, dynamic therapy, and radiation therapy. Treatment-induced tissue damage would strengthen the targeted immune cell–hitchhiking delivery nanomedicine. Therefore, this study not only provides the first in vivo cell-hitchhiking drug delivery systems with minimal premature loss of nanomedicine but also offers important new insights on new strategies for significantly improving tumor targeting efficiency of immune cell–based carriers.

MATERIALS AND METHODS

Experimental design

The objective of this study was to develop an in vivo strategy to construct immune cell–based carrier for enhanced tumor-targeted delivery of nanomedicine and improved antitumor immunotherapy. To achieve this goal, we first designed M-CD-GNPs and M-ADA-NPs and confirmed selective phagocytosis and subsequent supramolecular self-assembly of the mixture of two types of NP via β-CD–ADA host-guest interactions in macrophages. We next verified the efflux inhibition behavior of intracellular GNP aggregates from macrophages and their photothermal efficacy against B16 cells. Subsequently, melanoma mice were constructed to investigate the selective phagocytosis of Mixtures by immune cells in vivo and the cell-hitchhiking delivery of NP to the tumor. Furthermore, an initial PTT treatment on the tumor enhanced the accumulation efficiency of immune cell–based carriers, and the antitumor immunotherapeutic efficacy of secondary PTT treatment was investigated, which was assisted by immune checkpoint inhibitor. In general, the sample size of $n = 3$ to 6 per group was used and determined to be the optimal size for statistical analyses, and experiments were repeated independently.

Materials

$HAuCl_4{\cdot}3H_2O$, sodium citrate, 1-adamantanethiol, Cy5-PEG (2k)-SH, and FITC-PEG (2k)-SH were all procured from Aladdin (China). Zhiyuan Biological Technology Co. Ltd. (China) provided mono(6-mercapto-6-deoxy)-β-CD. Fetal bovine serum (FBS) and Gibco Dulbecco's modified Eagle's medium (DMEM) were obtained from Gibco (China). All other chemical reagents were supplied by Aladdin (China).

B16 cells, LO2 cells, and RAW264.7 cells were obtained from American Type Culture Collection (ATCC; USA). All of these cell lines were authenticated by DNA fingerprinting, isozyme detection, viability test, and mycoplasma detection. *E. coli* (ATCC 33694) was purchased from ATCC. Male C57BL/6 mice (6 weeks) were purchased from Faculty of Health Sciences, University of Macau. All animal procedures were approved by the Animal Ethics Committee, University of Macau and were conducted in accordance with the Animal Management Rules of the Ministry of Health of the P. R. China.

Preparation of GNPs

$HAuCl_4$ solution (0.25 mM, 100 ml) was put into a round bottomed flask and stirred under 130°C in oil bath. When the solution was boiled, the sodium citrate solution (0.7 ml, 5%) was added opportunely. Upon the color of reaction solution became wine red, the sodium citrate solution was added again, and the above process was repeated twice. Last, the solution was cooled to ambient temperature, and the GNPs were centrifuged at 12,850*g* for 30 min. After washing twice with deionized water, purified GNPs were collected and characterized by TEM, SEM, and DLS.

Preparation of CD-GNPs, ADA-GNPs, and GNP aggregates

For the preparation of CD-GNPs, the β-CD solution (5 mM, 2 ml) was added to 2 ml of concentrated GNP solution and stirred for 2 hours in room temperature. Then, the resultant solution was centrifuged at 21,000*g* for 8 min and dried for further use. Similarly, to preparing the ADA-GNPs, 0.015 mmol of ADA-SH was dissolved in 3 ml of dimethyl sulfoxide and then mixed with the concentrated GNPs for 2 hours. The obtained ADA-GNPs were further purified through centrifugation at 21,000*g* for 8 min and dried. CD-GNPs and ADA-GNPs were mixed in deionized water to prepare GNP aggregates and imaged by an optic camera. The morphology of GNP aggregates was detected by TEM and SEM. Ultraviolet-visible(UV-vis) absorption of GNP aggregates was measured by a UV spectrophotometer (DR6000, Hach), and the temperature change was recorded under NIR irradiation of 808 nm (0.5 W/cm^2) for 10 min.

PTT efficacy of GNP aggregates against B16 cells

B16 cells were cultured in a 75-cm^2 flask in DMEM with 10% (v/v) FBS at 37°C and incubated in DMEM containing GNPs, CD-GNPs, ADA-GNPs, and CD-GNPs + ADA-GNPs (molar ratio was 1:1) at a total Au of 0.2 mg/ml [the quantity of Au in each cell was determined by inductively coupled plasma mass spectrometry (ICP-MS)] for 6 hours. Then, the cell culture medium was irradiated for 5 min with an 808-nm laser, 3-(4,5-Dimethylthiazol-2-yl)-2,5-Diphenyltetrazolium Bromide (MTT) was added after treatment for 24 hours, and the absorbance was recorded by enzyme-labeled instrument (SpectraMax M5, Molecular Devices). Annexin V–FITC/ propidium iodide (PI) was also added and the fluorescence of FITC and PI was detected by a flow cytometer (CytoFLEX, Beckman Coulter). In addition, 2′-7′dichlorofluorescin diacetate (DCFH-DA) was incubated with cells after incubation for further 6 hours after NIR irradiation, and the fluorescence of DCF was determined by a flow cytometer.

ICD of B16 cells induced by PTT of GNP aggregates

B16 cells were cultured in flasks (25 cm^2) in DMEM that contained 10% (v/v) FBS at 37°C. Then, B16 cells were incubated with GNPs, CD-GNPs, ADA-GNPs, and their mixtures in DMEM, respectively, at a dosage of 0.2 mg/ml GNPs for 6 hours. After irradiation by an NIR laser for 5 min, the medium was collected for the analysis of HMGB-1 and ATP release via ELISA. The treated cells were collected and incubated with Alexa Fluor 488-CRT antibody for 2 hours. Then, the cells were further stained for 15 min with 4′,6-diamidino-2-phenylindole (DAPI). Subsequently, fluorescence images were taken by CLSM (TCS SP8, Leica), using 405- and 488-nm lasers to visualize the nuclei and CRT expression on the cell membrane, respectively. Quantitative analysis was conducted by a flow cytometer to further identify CRT exposure. In addition, B16 cells treated for 3 hours with mixtures of CD-GNPs and ADA-GNPs (at a dosage of 0.2 mg/ml GNPs in total) were imaged by CLSM to study the extracellular or intracellular location of the GNP aggregates.

Preparation of M-CD-GNPs and M-ADA-GNPs

E. coli was incubated overnight and centrifuged for 5 min at 2000*g*, and the subsequent supernatant was filtered with a 0.45-μm membrane. The resulting solution was transferred into Millipore with 10-kDa filter and centrifuged for 5 min at 5000*g* to obtain the OMV-rich solution. Last, the concentrated OMV solution was centrifuged at ultrahigh speed of 150,000*g* (Optima XPN-100 Ultracentrifuge, Beckman) for 3 hours, and the precipitant of OMVs was stored at −80°C for future investigations.

After collection of OMVs, the CD-GNPs and ADA-GNPs were added individually and sonicated 10 s at intervals of 10 s in sonication bath at a frequency of 40 kHz (100 W) for 2 min. Then, the subsequent solution was centrifuged for 30 min at 5000*g* to precipitate M-CD-GNPs and M-ADA-GNPs. The morphology of M-CD-GNPs and M-ADA-GNPs was studied by a TEM, and the sizes were analyzed by DLS [Nano-ZS Zetasizer, Malvern, and Zetasizer Software (version 7.11)]. The solution of Mixture was imaged by an optic camera, and the UV absorbance was determined by UV-vis spectrophotometry (DR6000, Hach). Furthermore, the proteins in the purified M-GNPs were analyzed via Coomassie Blue staining. The LPS content was analyzed by ELISA assay.

Cellular uptake toward GNPs and M-GNPs

RAW264.7 cells and L-02 cells were cultured in confocal dishes in DMEM containing 10% (v/v) FBS at 37°C and then individually incubated in DMEM with Cy5-GNPs and M-Cy5-GNPs at a total Au concentration of 0.2 mg/ml for different time points (1, 3, 6, and 9 hours). Then, the cells were fixed by paraformaldehyde, and the fluorescence photography was imaged by CLSM. ICP-MS (iCAP Q ICPMS, Thermo Fisher Scientific) was further used for quantitative analysis on the Au content inside the cells.

Intracellular assembly in RAW264.7 cells

RAW264.7 cells were cultured in 55-cm^2 dishes in DMEM containing 10% (v/v) FBS at 37°C and then individually incubated in DMEM with M-CD-GNPs, M-ADA-GNPs, and Mixture at a total concentration of 0.2 mg/ml of Au for 1, 3, 6, and 9 hours, and the cells were washed with PBS and fluorescence photography was imaged by CLSM. The intracellular Au content was further determined by ICP-MS.

Reflux behavior of RAW264.7 cells toward intracellular GNP aggregates

RAW264.7 cells were cultured in 55-cm^2 dishes in DMEM containing 10% (v/v) FBS at 37°C and then individually incubated in DMEM with M-Cy5-CD-GNPs, M-FITC-ADA-GNPs, and Mixture at a total Au concentration of 0.2 mg/ml for 6 hours. After washing twice with PBS and replacement with fresh media, the mass of Au remained in Raw264.7 cells was determined at different time points (1, 6, 12 and 24 hours) by ICP-MS, and the fluorescence photography was imaged by CLSM (TCS SP8, Leica).

Effect of intracellular GNP aggregates on macrophage

In vitro cytotoxicity of M-CD-GNPs and M-ADA-GNPs was evaluated via MTT assays. Briefly, RAW264.7 cells were cultured in 96-well plates and incubated with different concentrations (50, 100, and 200 μM Au) of M-CD-GNPs, M-ADA-GNPs, and Mixture for 24 hours. Then, the medium was replaced with DMEM, and the survival cells were quantified via MTT enzyme-linked immunometric meter (SpectraMax M5, Molecular Devices).

Transwell experiments were conducted to examine the migration ability and invasion ability of macrophage after intracellular supramolecular assembly of GNPs, in comparison to the free macrophage. Briefly, macrophages were seeded in a 24-well plate at 5×10^5 cells per well and incubated with Mixture at 0.2 mg/ml of Au for 6 hours. Then, macrophages loaded with GNP aggregates were plated onto 8-μm pore polycarbonate, and B16 cells were incubated in the bottom of a 24-well plate at 5×10^5 cells per well. After inserting to the 24-well plate and migrating for another 24 hours, cells on the top of each insert

were removed gently, and cells from the bottom were stained with crystal violet (0.1%) and photographed by microscopy (Migration-IX73). The free macrophages seeded in the 24-well plate were served as positive control. Through the similar procedures, the invasion experiment was conducted by dipping a layer of matric gel in the lower side of each insert. Then, the fluorescence photograph was imaged by Leica (Leica DMI8 living cell microscope).

Polarization effect of Mixture on macrophages

RAW264.7 cells were cultured in 55-cm^2 dishes in DMEM containing 10% (v/v) FBS at 37°C and then individually incubated in DMEM with M-β-CD-GNPs, M-ADA-GNPs, and Mixture (molar ratio was 1:1) at 0.2 mg/ml of Au for 6 hours. After PBS rinsing for twice, the cells were incubated for another 24 hours and stained with FITC-CD86 antibody for flow cytometry analysis (Cytoflex, Beckman Coulter).

In vivo hitchhiking delivery of Mixture in melanoma mice

Six-week-old C57BL/6 mice (male) were injected subcutaneously with 2×10^5 cells in 0.1 ml of PBS at the bottom right hind leg. Until the diameter of tumor size increased to 0.5 cm^2, the B16 tumor–bearing mice were used for further experiment. B16 tumor–bearing mice were intravenously injected with Cy5-GNPs, M-Cy5-GNPs, and M-Cy5-Mixture (n = 3), at a Cy5 dose of 0.5 mg/kg. After administration for 1 and 24 hours, the blood was collected and centrifuged to separate the leukocyte. The amount of leukocyte was calculated under a microscope and dissolved in aqua regia for the determination of Au content by ICP-MS (iCAP Q ICPMS, Thermo Fisher Scientific). Furthermore, the blood samples were incubated with FITC-CD11b antibody and PE-CD11c for 1.5 hours, and the fluorescence intensity of Cy5 in $CD11b^+$ cells and $CD11c^+$ cells was measured, respectively, by flow cytometry (Cytoflex, Beckman Coulter). Moreover, another batch of melanoma mouse was also intravenously administered with different GNP formulations (n = 3) and imaged by IVIS (Lumina XR, PerkinElmer) after administration for 1, 2, 3, 4, 6, 9, 12, and 24 hours. To analyze the pharmacokinetics of these GNP formulation, the blood samples (n = 3) were collected from melanoma mice after administration for 1, 2, 3, 4, 6, 9, 12, and 24 hours and imaged by IVIS. At the end point of experiment (24 hours), the heart, liver, spleen, lung, kidney, and tumor tissue were collected and ex vivo–imaged by IVIS. In addition, the TEM imaging was conducted on tumor tissues to observe the morphology of GNP aggregates, and the fluorescence imaging was used to detect the aggregated fluorescent signal of GNP aggregates in tumor tissues.

PTT treatment of Mixture-induced tumor inflammation

B16 tumor–bearing mice were administered with GNPs, M-GNPs, and Mixture at a total Au dose of 2 mg/kg. After administration for 1 hour, the mice were irradiated by an 808-nm laser (808, Hi-Tech Optoelectronics Co. Ltd.) for 5 min at 0.5 W/cm^2 power and were imaged by a photothermal imager (TiS60+, Fluke) at different time points (0.5, 1, 1.5, 2, 2.5, 3, 3.5, 4, 4.5, and 5 min). The tumor tissues were subsequently collected and imaged by a photothermal imager. Furthermore, after the initial PTT treatment at 1 hour after administration, the tumor tissues were harvested, and the level of TNF-α and IL-1β was measured by ELISA kit. Similarly, after administration for different hours (1, 2, 3, 4, 6, 9, 12, and 24 hours), the mice were irradiated for 5 min by an 808-nm laser of 0.5 W/cm^2 and imaged by a photothermal imager at the end of irradiation, and the tumor tissues were collected at preset time points to measure the tumor TNF-α level. At the end point of experiment (24 hours), the heart, liver, spleen, lung, kidney, and tumor tissue were collected and ex vivo–imaged by IVIS.

Antitumor therapy of Mixture with secondary PTT treatment

The PTT-induced antitumor therapy was conducted via two steps of irradiation by an 808-nm laser. Briefly, The B16 tumor–bearing mice were administered with GNPs, M-GNPs, and Mixture at an Au dose of 2 mg/kg. After administration for 1 hour, the mice were irradiated for 5 min by an 808-nm laser of 0.5 W/cm^2. After administration for 4 hours, the mice were irradiated 5 min again with an 808-nm laser of 0.5 W/cm^2. In Mixture-treated group, 8 μg of aPD-L1 per mouse was intravenously injected to the mice once every 3 days for five doses in total after administration of Mixture. The size of tumor tissues in all groups was recorded. After administration for 6 days, the tumor tissues were collected and imaged by a photo camera and sectioned for H&E staining, caspase-3 staining, and TUNEL staining. The lung tissues were harvested by analyzing the tumor metastasis, and the number of tumor metastatic sphere was recorded.

Infiltration of immune cells in tumor tissues

To examine the immunotherapy of Mixture, immunofluorescence analysis was performed on tumor sections. Briefly, frozen tumor sections were conducted with a thickness of 5 μm. Then, the sections were fixed in acetone at −20°C for 10 min and blocked with 2% bovine serum albumin for 1 hour. After PBS washing, the sections were stained by the following antibody groups for 1.5 hours: APC-F4/80 antibody, FITC-labeled CD11b antibody, allophycocyanin (APC)-CD3 antibody, and PE-CD8a antibody. After staining with DAPI for 10 min, the fluorescence photos were observed under CLSM.

To quantitatively analyze immune cells, the tumor tissue was treated for 1 hour with collagenase I (1 mg/ml). Then, the ground mixture was filtered through a nylon mesh filter to obtain suspension of single cells, which was subsequently incubated with APC-F4/80 antibody, FITC-labeled CD11b antibody and PerCP/Cyanine5.5-CD86, FITC-CD11b antibody, APC-CD45 antibody and PE-CD11c antibody, APC-CD3 antibody, and FITC-CD4 antibody and PE-CD8a antibody, respectively. A flow cytometer is used for cell collection, and FlowJo software is used for data analysis.

Safety evaluation

To evaluate the safety of Mixture, the normal mice were intravenously injected with 10-fold of Mixture used in antitumor study. After administration with Mixture for 1 and 24 hours, the blood was collected for white blood cell count by a hemocytometer, and the serum was collected for the determination on the level of inflammatory cytokines (TNF-α and IL-6), ALT, AST, BUN, and UA. The organs (heart, liver, spleen, lung, and kidney) were harvested after administration for 24 hours, and the histological examinations were performed.

Statistical analysis

Statistical analysis relied on one-way and two-way analysis of variance (ANOVA) methods. Statistical significance was annotated with $^*P \leq 0.05$, $^{**}P \leq 0.01$, and $^{***}P \leq 0.001$, respectively. All data were presented as the mean value ± SD of independent runs.

SUPPLEMENTARY MATERIALS

Supplementary material for this article is available at https://science.org/doi/10.1126/sciadv.abn1805

REFERENCES AND NOTES

1. J. S. Brenner, D. C. Pan, J. W. Myerson, O. A. Marcos-Contreras, C. H. Villa, P. Patel, H. Hekierski, S. Chatterjee, J.-Q. Tao, H. Parhiz, Red blood cell-hitchhiking boosts delivery of nanocarriers to chosen organs by orders of magnitude. *Nat. Commun.* **9**, 2684 (2018).
2. C. Wang, W. Sun, Y. Ye, Q. Hu, H. N. Bomba, Z. Gu, In situ activation of platelets with checkpoint inhibitors for post-surgical cancer immunotherapy. *Nat. Biomed. Eng.* **1**, 0011 (2017).
3. H.-H. Wu, Y. Zhou, Y. Tabata, J.-Q. Gao, Mesenchymal stem cell-based drug delivery strategy: From cells to biomimetic. *J. Control. Release* **294**, 102–113 (2019).
4. D. Wen, J. Wang, G. Van Den Driessche, Q. Chen, Y. Zhang, G. Chen, H. Li, J. Soto, M. Liu, M. Ohashi, Z. Wang, P. Abdou, Q. Hu, G. Dotti, S. Li, D. Fourches, Z. Gu, Adipocytes as anticancer drug delivery depot. *Matter* **1**, 1203–1214 (2019).
5. Y. Qiu, K. Ren, W. Zhao, Q. Yu, R. Guo, J. He, L. Mei, Y. Liu, J. Tang, S. Xu, J. Li, J. Wei, M. Li, Z. Zhang, Q. He, A "dual-guide" bioinspired drug delivery strategy of a macrophage-based carrier against postoperative triple-negative breast cancer recurrence. *J. Control. Release* **329**, 191–204 (2021).
6. L. Tang, Y. Zheng, M. B. Melo, L. Mabardi, A. P. Castaño, Y.-Q. Xie, N. Li, S. B. Kudchodkar, H. C. Wong, E. K. Jeng, M. V. Maus, D. J. Irvine, Enhancing T cell therapy through TCR-signaling-responsive nanoparticle drug delivery. *Nat. Biotechnol.* **36**, 707–716 (2018).
7. A. Ukidve, Z. Zhao, A. Fehnel, V. Krishnan, D. C. Pan, Y. Gao, A. Mandal, V. Muzykantov, S. Mitragotri, Erythrocyte-driven immunization via biomimicry of their natural antigen-presenting function. *Proc. Natl. Acad. Sci. U.S.A.* **117**, 17727–17736 (2020).
8. N. L. Klyachko, R. Polak, M. J. Haney, Y. Zhao, R. J. G. Neto, M. C. Hill, A. V. Kabanov, R. E. Cohen, M. F. Rubner, E. V. Batrakova, Macrophages with cellular backpacks for targeted drug delivery to the brain. *Biomaterials* **140**, 79–87 (2017).
9. X. Chang, L. Xing, Y. Wang, C.-X. Yang, Y.-J. He, T.-J. Zhou, X.-D. Gao, L. Li, H.-P. Hao, H.-L. Jiang, Monocyte-derived multipotent cell delivered programmed therapeutics to reverse idiopathic pulmonary fibrosis. *Sci. Adv.* **6**, eaba3167 (2020).
10. T. Shum, H. E. Heslop, A backpack revs up T-cell activity. *Nat. Biotechnol.* **36**, 702–703 (2018).
11. J. Xue, Z. Zhao, L. Zhang, L. Xue, S. Shen, Y. Wen, Z. Wei, L. Wang, L. Kong, H. Sun, Q. Ping, R. Mo, C. Zhang, Neutrophil-mediated anticancer drug delivery for suppression of postoperative malignant glioma recurrence. *Nat. Nanotechnol.* **12**, 692–700 (2017).
12. Q. Hu, W. Sun, J. Wang, H. Ruan, X. Zhang, Y. Ye, S. Shen, C. Wang, W. Lu, K. Cheng, G. Dotti, J. F. Zeidner, J. Wang, Z. Gu, Conjugation of haematopoietic stem cells and platelets decorated with anti-PD-1 antibodies augments anti-leukaemia efficacy. *Nat. Biomed. Eng.* **2**, 831–840 (2018).
13. C. Gao, Q. Cheng, J. Wei, C. Sun, S. Lu, C. H. Kwong, S. M. Lee, Z. Zhong, R. Wang, Bioorthogonal supramolecular cell-conjugation for targeted hitchhiking drug delivery. *Mater. Today* **40**, 9–17 (2020).
14. Y. Xia, L. Rao, H. Yao, Z. Wang, P. Ning, X. Chen, Engineering macrophages for cancer immunotherapy and drug delivery. *Adv. Mater.* **32**, 2002054 (2020).
15. C. Gao, Q. Huang, C. Liu, C. H. Kwong, L. Yue, J.-B. Wan, S. M. Lee, R. Wang, Treatment of atherosclerosis by macrophage-biomimetic nanoparticles via targeted pharmacotherapy and sequestration of proinflammatory cytokines. *Nat. Commun.* **11**, 2622 (2020).
16. W. Zhang, M. Wang, W. Tang, R. Wen, S. Zhou, C. Lee, H. Wang, W. Jiang, I. M. Delahunty, Z. Zhen, H. Chen, M. Chapman, Z. Wu, E. W. Howerth, H. Cai, Z. Li, J. Xie, Nanoparticle-laden macrophages for tumor-tropic drug delivery. *Adv. Mater.* **30**, 1805557 (2018).
17. T. Deuse, X. Hu, A. Gravina, D. Wang, G. Tediashvili, C. De, W. O. Thayer, A. Wahl, J. V. Garcia, H. Reichenspurner, M. M. Davis, L. L. Lanier, S. Schrepfer, Hypoimmunogenic derivatives of induced pluripotent stem cells evade immune rejection in fully immunocompetent allogeneic recipients. *Nat. Biotechnol.* **37**, 252–258 (2019).
18. F. Mo, N. Watanabe, M. K. McKenna, M. J. Hicks, M. Srinivasan, D. Gomes-Silva, E. Atilla, T. Smith, P. A. Atilla, R. Ma, D. Quach, H. E. Heslop, M. K. Brenner, M. Mamonkin, Engineered off-the-shelf therapeutic T cells resist host immune rejection. *Nat. Biotechnol.* **39**, 56–63 (2021).
19. J. Choi, H.-Y. Kim, E. J. Ju, J. Jung, J. Park, H.-K. Chung, J. S. Lee, J. S. Lee, H. J. Park, S. Y. Song, S.-Y. Jeong, E. K. Choi, Use of macrophages to deliver therapeutic and imaging contrast agents to tumors. *Biomaterials* **33**, 4195–4203 (2012).
20. M. Hao, S. Hou, W. Li, K. Li, L. Xue, Q. Hu, L. Zhu, Y. Chen, H. Sun, C. Ju, C. Zhang, Combination of metabolic intervention and T cell therapy enhances solid tumor immunotherapy. *Sci. Transl. Med.* **12**, eaaz6667 (2020).
21. D. Chu, X. Dong, X. Shi, C. Zhang, Z. Wang, Neutrophil-based drug delivery systems. *Adv. Mater.* **30**, 1706245 (2018).
22. K. K. Chaudagar, N. Landon-Brace, A. Solanki, H. M. Hieromnimon, E. Hegermiller, W. Li, Y. Shao, J. Joseph, D. J. Wilkins, K. M. Bynoe, X.-L. Li, J. G. Clohessy, S. Ullas, J. M. Karp, A. Patnaik, Cabozantinib unlocks efficient in vivo targeted delivery of neutrophil-loaded nanoparticles into murine prostate tumors. *Mol. Cancer Ther.* **20**, 438–449 (2021).
23. I. Aiello, M. M. Fedele, F. Román, L. Marpegan, C. Caldart, J. J. Chiesa, D. A. Golombek, C. Finkielstein, N. Paladino, Circadian disruption promotes tumor-immune microenvironment remodeling favoring tumor cell proliferation. *Sci. Adv.* **6**, eaaz4530 (2020).
24. Y. M. Zhang, Y. H. Liu, Y. Liu, Cyclodextrin-based multistimuli-responsive supramolecular assemblies and their biological functions. *Adv. Mater.* **32**, 1806158 (2020).
25. R. Lanza, D. W. Russell, A. Nagy, Engineering universal cells that evade immune detection. *Nat. Rev. Immunol.* **19**, 723–733 (2019).
26. C. Yang, K. Bromma, W. Sung, J. Schuemann, D. Chithrani, Determining the radiation enhancement effects of gold nanoparticles in cells in a combined treatment with cisplatin and radiation at therapeutic megavoltage energies. *Cancer* **10**, 150 (2018).
27. D.-B. Grys, B. de Nijs, A. R. Salmon, J. Huang, W. Wang, W.-H. Chen, O. A. Scherman, J. J. Baumberg, Citrate coordination and bridging of gold nanoparticles: The role of gold adatoms in AuNP aging. *ACS Nano* **14**, 8689–8696 (2020).
28. S. Loescher, A. Walther, Supracolloidal self-assembly of divalent janus 3D DNA origami via programmable multivalent host/guest interactions. *Angew. Chem. Int. Edit.* **59**, 5515–5520 (2020).
29. M. Kielbik, I. Szulc-Kielbik, M. Klink, Calreticulin—Multifunctional chaperone in immunogenic cell death: Potential significance as a prognostic biomarker in ovarian cancer patients. *Cell* **10**, 130 (2021).
30. X. Duan, C. Chan, W. Han, N. Guo, R. R. Weichselbaum, W. Lin, Immunostimulatory nanomedicines synergize with checkpoint blockade immunotherapy to eradicate colorectal tumors. *Nat. Commun.* **10**, 1899 (2019).
31. Z. Asadzadeh, E. Safarzadeh, S. Safaei, A. Baradaran, A. Mohammadi, K. Hajiasgharzadeh, A. Derakhshani, A. Argentiero, N. Silvestris, B. Baradaran, Current approaches for combination therapy of cancer: The role of immunogenic cell death. *Cancer* **12**, 1047 (2020).
32. J. D. Van Belleghem, K. Dąbrowska, M. Vaneechoutte, J. J. Barr, P. L. Bollyky, Interactions between bacteriophage, bacteria, and the mammalian immune system. *Viruses* **11**, 10 (2019).
33. S. Muñoz-Sánchez, M. van der Vaart, A. H. Meijer, Autophagy and Lc3-associated phagocytosis in zebrafish models of bacterial infections. *Cell* **9**, 2372 (2020).
34. S. H. Kaufmann, A. Dorhoi, Molecular determinants in phagocyte-bacteria interactions. *Immunity* **44**, 476–491 (2016).
35. S. Thamphiwatana, P. Angsantikul, T. Escajadillo, Q. Zhang, J. Olson, B. T. Luk, S. Zhang, R. H. Fang, W. Gao, V. Nizet, L. Zhang, Macrophage-like nanoparticles concurrently absorbing endotoxins and proinflammatory cytokines for sepsis management. *Proc. Natl. Acad. Sci. U.S.A.* **114**, 11488–11493 (2017).
36. M. Reyes, M. R. Filbin, R. P. Bhattacharyya, K. Billman, T. Eisenhaure, D. T. Hung, B. D. Levy, R. M. Baron, P. C. Blainey, M. B. Goldberg, N. Hacohen, An immune-cell signature of bacterial sepsis. *Nat. Med.* **26**, 333–340 (2020).
37. M. P. Kai, H. E. Brighton, C. A. Fromen, T. W. Shen, J. C. Luft, Y. E. Luft, A. W. Keeler, G. R. Robbins, J. P. Ting, W. C. Zamboni, J. E. Bear, J. M. DeSimone, Tumor presence induces global immune changes and enhances nanoparticle clearance. *ACS Nano* **10**, 861–870 (2016).
38. N. Benne, J. van Duijn, J. Kuiper, W. Jiskoot, B. Slütter, Orchestrating immune responses: How size, shape and rigidity affect the immunogenicity of particulate vaccines. *J. Control. Release* **234**, 124–134 (2016).
39. G. Yang, S. Z. F. Phua, A. K. Bindra, Y. Zhao, Degradability and clearance of inorganic nanoparticles for biomedical applications. *Adv. Mater.* **31**, 1805730 (2019).
40. B. Du, M. Yu, J. Zheng, Transport and interactions of nanoparticles in the kidneys. *Nat. Rev. Mater.* **3**, 358–374 (2018).
41. C. Gao, Q. Cheng, J. Li, J. Chen, Q. Wang, J. Wei, Q. Huang, S. M. Lee, D. Gu, R. Wang, Supramolecular macrophage-liposome marriage for cell-hitchhiking delivery and immunotherapy of acute pneumonia and melanoma. *Adv. Funct. Mater.* **31**, 2102440 (2021).
42. S. Gujar, J. G. Pol, Y. Kim, P. W. Lee, G. Kroemer, Antitumor benefits of antiviral immunity: An underappreciated aspect of oncolytic virotherapies. *Trends Immunol.* **39**, 209–221 (2018).
43. P. Tsou, H. Katayama, E. J. Ostrin, S. M. Hanash, The emerging role of B cells in tumor immunity. *Cancer Res.* **76**, 5597–5601 (2016).
44. W. Zhang, M. Zi, L. Sun, F. Wang, S. Chen, Y. Zhao, S. Liang, J. Hu, S. Liu, L. Liu, Y. Zhan, Z. M. Lew, Y. Xu, Cystatin C regulates major histocompatibility complex-II–peptide presentation and extracellular signal-regulated kinase-dependent polarizing cytokine production by bone marrow-derived dendritic cells. *Immunol. Cell Biol.* **97**, 916–930 (2019).
45. X. Zhang, J. Tang, C. Li, Y. Lu, L. Cheng, J. Liu, A targeting black phosphorus nanoparticle based immune cells nano-regulator for photodynamic/photothermal and photo-immunotherapy. *Bioact. Mater.* **6**, 472–489 (2021).
46. M. R. Pulido, M. García-Quintanilla, J. Pachón, M. J. McConnell, A lipopolysaccharide-free outer membrane vesicle vaccine protects against Acinetobacter baumannii infection. *Vaccine* **38**, 719–724 (2020).
47. C. Irene, L. Fantappiè, E. Caproni, F. Zerbini, A. Anesi, M. Tomasi, I. Zanella, S. Stupia, S. Prete, S. Valensin, E. König, L. Frattini, A. Gagliardi, S. J. Isaac, A. Grandi, G. Guella,

G. Grandi, Bacterial outer membrane vesicles engineered with lipidated antigens as a platform for *Staphylococcus aureus* vaccine. *Proc. Natl. Acad. Sci. U.S.A.* **116**, 21780–21788 (2019).

Acknowledgments: We thank the State Key Laboratory of Quality Research in Chinese Medicine (University of Macau) and MoE Frontiers Science Center for Precision Oncology for providing the fundamental experimental facilities. **Funding:** This work was supported by Dr. Stanley Ho Medical Development Foundation (grant no.: SHMDF-OIRFS/2021/002), Science and Technology Development Fund (FDCT), Macau SAR (grant no.: 0065/2021/A2), and National Natural Science Foundation of China (22071275 and 32001016). **Author contributions:** Conceptualization: R.W. and C.G. Methodology: C.G., Q.W., and J.L. Investigation: J.W., C.H.T.K., B.X., and S.L. Supervision: R.W. and S.M.Y.L. Writing—original draft: R.W. and C.G. Writing—review and editing: R.W. and CG. **Competing interests:** The authors declare that they have no competing interests. **Data and materials availability:** All data needed to evaluate the conclusions in the paper are present in the paper and/or the Supplementary Materials.

Submitted 9 November 2021
Accepted 29 March 2022
Published 11 May 2022
10.1126/sciadv.abn1805